

Algorithms for Advanced Battery-Management Systems

MODELING, ESTIMATION, AND CONTROL CHALLENGES FOR LITHIUM-ION BATTERIES

NALIN A. CHATURVEDI,
REINHARDT KLEIN,
JAKE CHRISTENSEN,
JASIM AHMED, and
ALEKSANDAR KOJIC

Lithium-ion (Li-ion) batteries are ubiquitous sources of energy for portable electronic devices. Compared to alternative battery technologies [1], [2], Li-ion batteries provide one of the best energy-to-weight ratios, exhibit no memory effect, and have low self-discharge when not in use. These beneficial properties, as well as decreasing costs, have established Li-ion batteries as a leading candidate for the next generation of automotive and aerospace applications [2].

In the automotive sector, increasing demand for hybrid electric vehicles (HEVs), plug-in HEVs (PHEVs), and EVs has pushed manufacturers to the limits of contemporary automotive battery technology. This limitation is gradually forcing consideration of alternative battery technologies, such as Li-ion batteries, as a replacement for existing lead-acid and nickel-metal-hydride batteries. Unfortunately, this replacement is a challenging task since automotive applications demand large amounts of energy and power and must operate safely, reliably, and durably at these scales.



In most applications, a battery system consists of the battery and the battery-management system (BMS). A BMS is composed of hardware and software that control the charging and discharging of the battery while guaranteeing reliable and safe operation [3]. The BMS also handles additional functions, such as cell balancing and thermal management of the battery pack. The design of a sophisticated BMS is necessary to ensure longevity and performance since battery behavior can change with time [4], [5]. Additionally, the BMS is critical for safety since Li-ion batteries can ignite and explode when overcharged [3], [6] or due to abuse [7].

Designing and building BMS software algorithms for Li-ion batteries require a model that can describe the battery dynamics. Indeed, one of the key tasks of the BMS software is to observe the states of the battery and track physical parameters as the battery ages. A typical BMS uses an equivalent circuit model [8]–[11]; however, these models have limited prediction capability compared to physics-based electrochemical models. In contrast, a defining feature of an advanced BMS is that it uses a physics-based electrochemical model instead of an equivalent circuit model.

In this article, we present a detailed description and model of a Li-ion battery. We begin the section “Intercalation-Based Batteries” by providing an intuitive explanation of the fundamentals behind storing energy in a Li-ion battery. In the sections “Modeling Approach” and “Li-Ion Battery Model,” we present equations that describe a Li-ion cell’s dynamic behavior. This modeling is based on using electrochemical principles to develop a physics-based model [12]–[17] in contrast to equivalent circuit models [8]–[11]. A goal of this article is to present the electrochemical model [12]–[17] from a controls perspective.

The electrochemical model presented in [12]–[17] can predict the spatially distributed behavior of the essential states of the battery, such as concentration of lithium ions, potentials in the electrolyte and the solid electrode material, and various safety-relevant quantities as the battery is *cycled*, that is, charged and discharged repeatedly. Knowledge of these quantities helps to determine the state of the battery as well as its ability to provide energy. Although equivalent circuit-based models can describe the behavior of some of these states, these models are based on small ac-signal perturbations of the battery [18] and thus have limited applicability. Ad hoc modifications of the equivalent circuit, in which the circuit parameters vary with the operating region, are used in practice [8], [11]. However, these models usually neglect mass-transfer limitations due to solid-phase diffusion, resulting in prediction errors when used over a wide operating region. In this article, we focus on electrochemical models.

In the section “Control and Estimation Challenges for Li-Ion Batteries,” we describe technical challenges that arise in ensuring safe and reliable operation of Li-ion

batteries. The goal is to convey the role of estimation and control algorithms for BMS in Li-ion battery technology. Simulation results for a simplified case illustrate how performance can be improved with knowledge of the states of the model. In the section “Framework for the Li-ion Battery Model,” we develop a reformulation of this model, which can be used to study the full Li-ion battery model and obtain reduced-order models. Note that the literature on modeling of Li-ion batteries [12]–[17] avoids these detailed constructions since their primary aim is to numerically simulate the behavior of Li-ion batteries to gain further understanding. However, if the intention is to build control or estimation algorithms for BMS, then a control-oriented understanding of the Li-ion battery model becomes imperative. Next, we use this framework to approximate the electrochemical Li-ion battery model. This approximation is also studied in [19] and [20].

In the section “Experimental and Simulation Results,” the full and approximate models are compared in both simulations and experiments. The simulation results are presented for both high-power and high-energy cell configurations. Based on the application and domain of operation, we identify the domains in which the approximate model, instead of the full model, can be used for BMS problems. In the last section, we review the status of research on BMS and the current solutions to estimation and control problems along with their advantages and disadvantages. We conclude by mentioning directions for future research.

INTERCALATION-BASED BATTERIES

The process of moving ions in and out of an interstitial site in a lattice is called *intercalation*. The commonly available Li-ion cell is a dual-intercalation cell, which means that both electrodes have lattice sites that can store lithium. Charging (discharging) a dual-intercalation cell causes the Li ions to leave the lattice sites in the positive (negative) electrode and enter the lattice sites of the negative (positive) electrode. The difference in energy states of the intercalated lithium in the positive and negative electrodes governs the energy stored in the Li-ion cell.

Working Principle of a Li-Ion Battery

A typical Li-ion battery has four main components (Figure 1). The *porous negative electrode* of a Li-ion cell is connected to the negative terminal of the cell. This electrode usually contains graphite, which is an intercalation material. Similarly, the *porous positive electrode* is connected to the positive terminal of the cell. The positive electrode can have various chemistries, but it is usually a metal oxide or a blend of multiple metal oxides, such as $\text{Li}_x\text{Mn}_2\text{O}_4$ and Li_xCoO_2 . A *separator* is a thin porous medium that separates the negative from the positive electrode. The separator is an electrical insulator that does not allow electrons to flow between the positive and negative electrodes. However, being porous, the separator allows ions to pass through it by

means of the electrolyte. The *electrolyte* is a concentrated solution that contains charged species. These charged species can move in response to an electrochemical potential gradient. Note that some Li-ion batteries have a solid electrolyte, which serves both as an ionic conducting medium and an electronically insulating separator. However, in both cases, the charged species that intercalates in the battery is the Li^+ ion and hence the name Li-ion battery. The negative electrode, positive electrode, and separator are all immersed in this electrolyte with the electrolyte filling all the pores of the solid material.

Electrodes of the Li-ion battery also contain material that acts as a conductive filler agent in the electrodes, as shown in Figure 1. While these materials do not intercalate lithium, they hold the electrode structure together, which improves the electronic conductivity of the electrodes. In addition, nonporous current collectors are present at each side of the cell sandwich to electrically connect the porous electrode structures to the cell terminals.

Open-Circuit Potentials

The key idea behind storing energy in a Li-ion cell is that the free energy of lithium when placed in an interstitial site of the positive electrode is different from the free energy when placed in an interstitial site of the negative electrode. In particular, compared to the positive electrode, lithium has much higher energy when stored in the negative electrode. For a given material, these free energies are known and related to electrochemical potentials. By using these values of the electrochemical potentials, we can express the electrostatic potential of a positive or negative electrode as a function of how much lithium is stored in the electrode. The lithium concentration in the electrode normalized by the maximum possible concentration is called the *utilization* of the electrode. Thus, the electrostatic potential of an electrode, referred to as the *open-circuit potential* (OCP) of the electrode, can be expressed as a function of the utilization of the electrode.

Note that both the negative and positive electrode have an OCP. Let $U^-(\xi^-)$ denote the OCP of the negative electrode, and let $U^+(\xi^+)$ denote the OCP of positive electrode, where the arguments ξ^- and ξ^+ represent the volume-averaged concentration in the respective electrode. Then, the difference $U^+(\xi^+) - U^-(\xi^-)$ is the OCP of the complete cell. The OCP of the cell is alternatively referred to as the open-circuit voltage. The OCP of the cell corresponds to the rest voltage measured across the current collectors, assuming no currents.

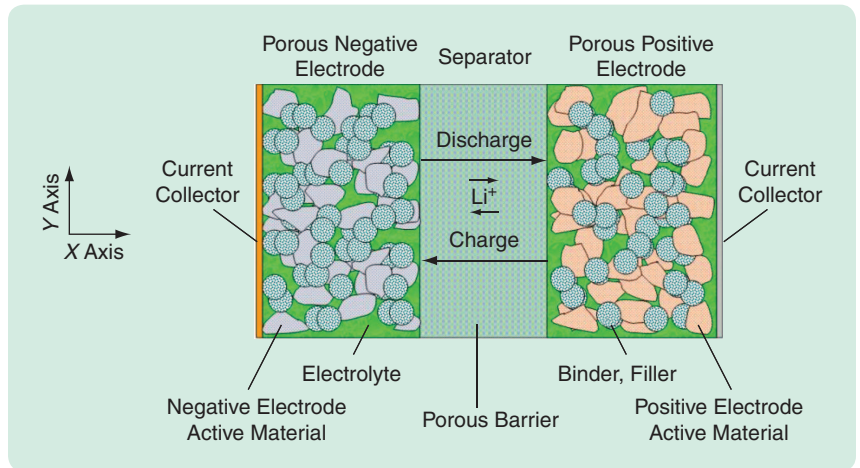


FIGURE 1 Anatomy of an intercalation cell. The positive and negative electrodes are separated by an insulating material (separator), which does not allow electrons to pass but is porous enough for lithium ions to flow. Also note the presence of additional conductive and binder materials in the electrodes. These materials hold the electrode together and improve its conductivity.

MODELING APPROACH

We now construct a dynamic model for a Li-ion battery using electrochemical principles. The one-dimensional (1D)-spatial model of a Li-ion battery considers dynamics along only one axis (the horizontal X-axis) and neglects the dynamics along the remaining two axes (Y-axis and Z-axis) [12]–[18]. This approximation is applicable to most cell structures with a large cross-sectional area and low currents. For example, the characteristic length scale of a typical Li-ion cell along the X-axis is on the order of $100 \mu\text{m}$, whereas the characteristic length scale for the remaining two axes is on the order of $100,000 \mu\text{m}$ or more.

In each domain of a Li-ion cell, namely, the negative electrode, separator, and positive electrode, lithium can be thought of as existing in two disjoint states, called *phases*. The first phase represents the intercalated lithium in the electrode material, whereas the second phase involves the lithium in a dissolved state in the electrolyte. Thus, for the Li-ion battery shown in Figure 1, lithium can exist at every point along the X-axis either in the solid phase in an interstitial site, or in the dissolved state in the electrolyte phase. Hence, a 1D-spatial model of a Li-ion battery can be represented as shown in Figure 2. In the separator domain, however, lithium exists only in the electrolyte phase. Equations are needed to describe the dynamics of each phase of lithium in the Li-ion battery.

We model the Li-ion cell by assuming, as shown in Figure 2, that spherical solid particles, denoting an agglomeration of lattice sites, exist everywhere along the X-axis. The intercalation process is then modeled by the insertion of lithium ions in and out of these spherical solid particles. These particles are immersed in the electrolyte as shown in Figure 2.

The state variables required to describe the 1D-spatial model at the position x at time t are the current $i_s(x, t)$ in the

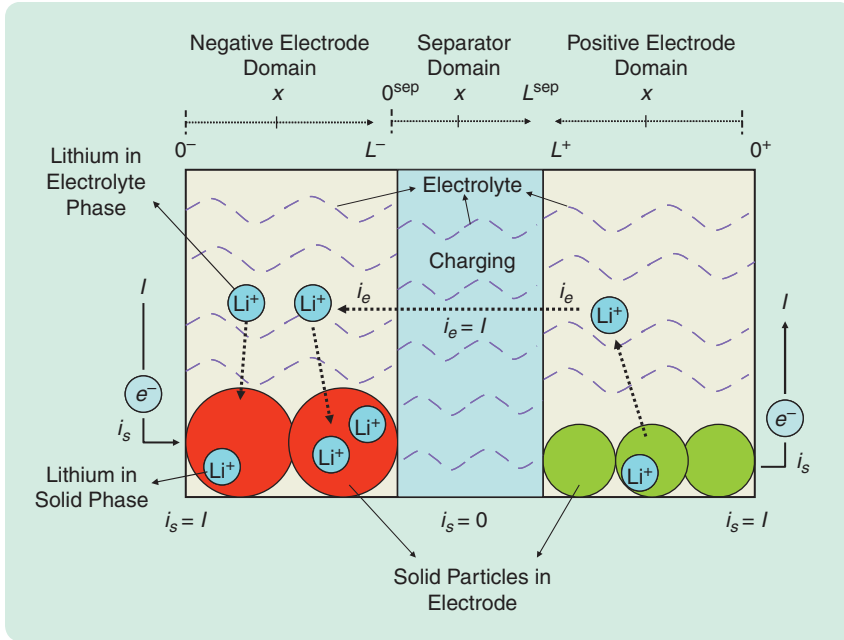


FIGURE 2 Simple schematic showing the modeling approach for an intercalation cell. In the X -dimension (horizontal axis), the cell is divided into three physical domains, namely, the positive electrode, the negative electrode, and the separator. Also, each electrode and the separator have their own coordinates for spatial definition of their respective domains given by $[0^+, L^+]$, $[0^-, L^-]$, and $[0^{\text{sep}}, L^{\text{sep}}]$ for the positive and negative electrode, and the separator, respectively. In each electrode domain, lithium can exist either in the solid phase in an interstitial site or in the electrolyte phase in a dissolved state. Thus, the lattice structure of an electrode in a Li-ion cell can be visualized as small spherical-solid particles that hold lithium ions in the solid phase; these solid spherical particles, which denote a collection of interstitial sites, are immersed in the electrolyte. The intercalation process can then be visualized as lithium ions moving in and out of these solid particles as the battery is charged or discharged. Note that the separator has lithium in only the electrolyte phase. Thus i_s , representing the electronic current in the solid particle, is zero in the separator, while the ionic current in the electrolyte, denoted by i_e , is equal to the applied current I in the separator.

solid electrode, the current $i_e(x, t)$ in the electrolyte, the electric potential $\Phi_s(x, t)$ in the solid electrode, the electric potential $\Phi_e(x, t)$ in the electrolyte, the molar flux $j_n(x, t)$ of lithium at the surface of the spherical particle, the concentration $c_e(x, t)$ of the electrolyte, and the concentration $c_s(x, r, t)$ of lithium in the solid phase at a distance r from the center of a spherical particle located at x in the solid electrode at time t (see Figure 3).

In the following development, the superscripts “+,” “-,” and “sep” imply that the variables are defined in the positive electrode, negative electrode, and separator domain, respectively. Each of these spatial domains spans $[0^+, L^+]$, $[0^-, L^-]$, and $[0^{\text{sep}}, L^{\text{sep}}]$, respectively, as shown in Figure 2. Thus, $c_e^+(x, t)$ denotes the concentration of lithium in the electrolyte at each $x \in [0^+, L^+]$ at time t . When not referring to a specific domain or when it is clear from context, we remove the superscript for simplicity of notation.

LI-ION BATTERY MODEL

We now present equations that describe the electrochemical behavior of a Li-ion battery. Before we proceed, we

note that all currents represent current densities normalized by the cross-sectional area of the separator. The input to the model is the external current density $I(t)$ applied to the battery, and the output of the model is the corresponding output voltage $V(t)$ given by

$$V(t) = \Phi_s(0^+, t) - \Phi_s(0^-, t), \quad (1)$$

where 0^+ and 0^- correspond to the two ends of the electrode sandwich shown in Figure 2.

Relationship Between Potential and Currents

Potential in the Solid Electrode

Combining Kirchoff's law $i_s + i_e = I$ with Ohm's law relating i_s and Φ_s , we obtain

$$\frac{\partial \Phi_s(x, t)}{\partial x} = \frac{i_e(x, t) - I(t)}{\sigma}, \quad (2)$$

where σ is the effective electronic conductivity of the entire electrode. Since the electrode is porous, only a fraction of the electrode's volume contributes to its electronic conductivity. Equation (2) has no explicit boundary conditions. However, at the interface between the electrode and current collector, we have $i_e(0^+, t) = i_e(0^-, t) = 0$,

whereas, at the electrode-separator interface, we have $i_e = I$. As shown in the section “Framework for the Li-Ion Battery Model,” we can choose either $i_e(0^+, t) = i_e(0^-, t) = 0$ or $i_e = I$ at the separator as the boundary condition for (2).

Potential in the Electrolyte

The relationship between Φ_e and i_e in the electrolyte is given by

$$\frac{\partial \Phi_e(x, t)}{\partial x} = -\frac{i_e(x, t)}{\kappa} + \frac{2RT}{F}(1 - t_e^0) \times \left(1 + \frac{d \ln f_{c/a}}{d \ln c_e}(x, t) \right) \frac{\partial \ln c_e(x, t)}{\partial x}, \quad (3)$$

where F is Faraday's constant, R is the universal gas constant, T is the temperature of the cell, and $f_{c/a}$ is the mean molar activity coefficient in the electrolyte. The dimensionless number $f_{c/a}$ which accounts for deviations of the electrolyte solution from ideal behavior, is a function of the electrolyte concentration. Also, κ is the ionic conductivity of

the electrolyte, and t_c^0 is the transference number of the cations with respect to the solvent velocity. Both κ and t_c^0 are usually functions of electrolyte concentration, but t_c^0 is typically approximated as a constant. Since we can measure only potential differences, the boundary condition of Φ_e is arbitrary. We set $\Phi_e(0^+, t) = 0$ at the positive electrode-current collector interface. For the remaining two domains, it follows from continuity of Φ_e that $\Phi_e(L^{\text{sep}}, t) = \Phi_e(L^+, t)$ and $\Phi_e(L^-, t) = \Phi_e(0^{\text{sep}}, t)$.

Relationship Between Concentrations and Currents

Transport in the Electrolyte

The lithium concentration in the electrolyte changes due to concentration-gradient-induced diffusive flow of ions and the current i_e . Thus, it can be shown that

$$\frac{\partial c_e(x, t)}{\partial t} = \frac{\partial}{\partial x} \left(D_e \frac{\partial c_e(x, t)}{\partial x} \right) + \frac{1}{F \varepsilon_e} \frac{\partial (t_a^0 i_e(x, t))}{\partial x}, \quad (4)$$

where D_e is the effective diffusion coefficient, ε_e is the volume fraction of the electrolyte, and t_a^0 is the transference number for the anion. The first term in (4) reflects the change in concentration due to diffusion, while the second term reflects the change in concentration due to the current i_e and its gradient. The boundary conditions for (4) capture the fact that the fluxes of the ions are zero for all time at the current collectors. Since the flux is proportional to the concentration gradient at the current collectors, we obtain

$$\frac{\partial c_e}{\partial x} \Big|_{x=0^-} = \frac{\partial c_e}{\partial x} \Big|_{x=0^+} = 0. \quad (5)$$

Since the battery has three spatial domains, we need four additional boundary conditions at the electrode-separator interface. These boundary conditions are obtained from continuity of the flux and concentration of the electrolyte at the electrode-separator interface (shown in Figure 2) as

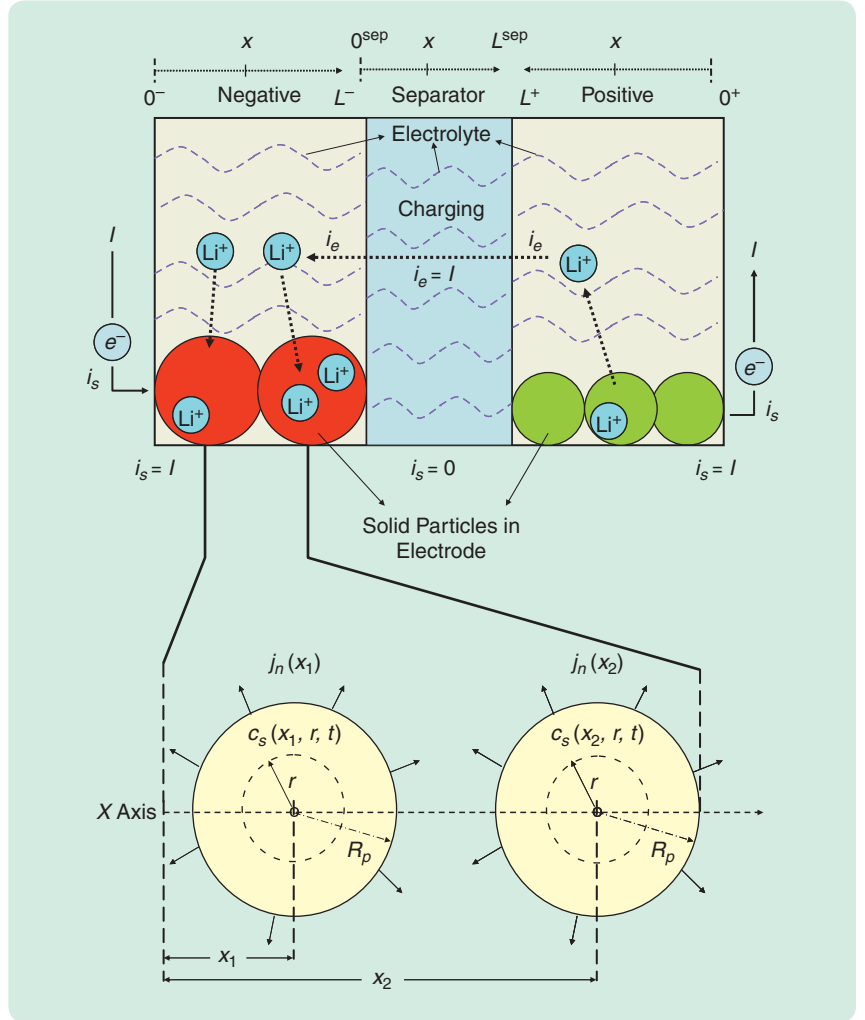


FIGURE 3 Modeling of molar flux $j_n(x)$ and the concentration of solid-phase lithium in the electrode. In this macro-homogeneous model, lithium concentration in the solid phase is modeled by using a densely populated distribution of spherical solid particles along the X -axis, each of which denotes a collection of interstitial sites. For each solid particle at x , the function $c_s(x, r, t)$ represents the concentration of lithium in the particle in the radial dimension at time t .

$$\varepsilon_e^- \left(D_e \frac{\partial c_e}{\partial x} \right) \Big|_{x=L^-} = \varepsilon_e^{\text{sep}} \left(D_e \frac{\partial c_e}{\partial x} \right) \Big|_{x=0^{\text{sep}}}, \quad (6)$$

$$\varepsilon_e^{\text{sep}} \left(D_e \frac{\partial c_e}{\partial x} \right) \Big|_{x=L^{\text{sep}}} = \varepsilon_e^+ \left(D_e \frac{\partial c_e}{\partial x} \right) \Big|_{x=L^+}, \quad (7)$$

$$c_e(L^-, t) = c_e(0^{\text{sep}}, t), \quad (8)$$

$$c_e(L^{\text{sep}}, t) = c_e(L^+, t). \quad (9)$$

Transport in the Solid Phase

As explained in the section “Modeling Approach,” the model in the solid phase associates a spherical particle of radius R_p with each spatial location x . The transport of the lithium ions in these solid particles can be described in a

Overpotential of a Reaction

In a Li-ion battery, the *overpotential* η_r of reaction r determines the rate of that reaction. For reactions that occur at the surface of the electrode and where lithium is the primary reactant, the overpotential η_r represents the deviation between the thermodynamic equilibrium potential difference at the existing surface concentration and the potential difference that a charged species would go through as it passes through the solid-electrolyte interphase (SEI) between the solid electrode and the electrolyte; see Figure 4 for a description of the overpotential corresponding

to the reaction of intercalation of lithium. As described in figures 3 and 4, the overpotential η_r is defined as

$$\eta_r(x, t) = \Phi_s(x, t) - \Phi_e(x, t) - U_r(c_{ss}(x, t)) - FR_f j_n(x, t),$$

$$c_{ss}(x, t) \triangleq c_s(x, R_p, t),$$

where R_f is the film resistance of the SEI, U_r denotes the equilibrium potential of the reaction, and j_n denotes the molar flux of the reaction [18], [16].

fashion similar to the transport of ions in the electrolyte. Thus solid phase transport of lithium can be described by an equation similar to (4), where the diffusion gradient is defined with respect to the spatial dimension of the spherical particle. However, for most battery materials of interest, diffusion is the dominating phenomenon involved in solid phase transport of lithium [15]. Thus, the transport of lithium ions in the electrode material is described by

$$\frac{\partial c_s(x, r, t)}{\partial t} = \frac{1}{r^2} \frac{\partial}{\partial r} \left(D_s r^2 \frac{\partial c_s(x, r, t)}{\partial r} \right), \quad (10)$$

where r is the radial dimension of the particles in the electrode, and D_s is the diffusion coefficient. The boundary and initial conditions are given by

$$\left. \frac{\partial c_s}{\partial r} \right|_{r=0} = 0, \quad (11)$$

$$\left. \frac{\partial c_s}{\partial r} \right|_{r=R_p} = -\frac{1}{D_s} j_n \quad (12)$$

$$c_s(x, r, 0) = c_s^0. \quad (13)$$

Equations (11) and (12) imply that, at the surface of the particles, the rate at which ions exit the particle and enter the electrolyte is given by the pore-wall molar flux $j_n(x)$, and this rate is zero at the center (see Figure 3). The initial condition (13) fits the initial concentration profile in the solid particle. Note that we neglect diffusion between adjacent particles. More precisely, we do not consider terms containing $\partial c_s / \partial x$ in (10) since they are negligible given the high solid phase diffusive impedance between particles.

Conservation of Charge

At each x in the electrode, the net pore-wall molar flux is related to the divergence of the current. Thus,

$$\frac{\partial i_e(x, t)}{\partial x} = aF j_n(x, t), \quad (14)$$

where the specific interfacial area $a \triangleq \varepsilon_s (4\pi R_p^2) / [(4/3)\pi R_p^3] = (3/R_p)\varepsilon_s$ and ε_s is the volume fraction of the solid electrode material in the porous electrode. The boundary condition is $i_e = 0$ at the current collectors, that is, $i_e(0^-, t) = i_e(0^+, t) = 0$, and $i_e(x, t) = I$ for all $x \in [0^{\text{sep}}, L^{\text{sep}}]$. Since the current in the separator is I , it follows that $i_e(L^+, t) = i_e(L^-, t) = I$. Thus, (14) has more than one boundary condition in the two electrode domains, thereby making it overconstrained. However, since (2) describing Φ_s does not have an explicit boundary condition, the total number of boundary conditions for the system of partial differential equations (PDEs) matches the required number of boundary conditions.

Butler-Volmer Kinetics

The molar flux j_n depends on the concentration c_s of lithium in the solid, the concentration c_e of lithium in the electrolyte, and the *solid-phase intercalation overpotential* η_s through the Butler-Volmer equation [18], [16]. The overpotential η_s corresponds to the reaction of solid-phase intercalation of lithium in the electrodes; see “Overpotential of a Reaction” and figures 3 and 4 for more details. The overpotential for the intercalation reaction is described as

$$\eta_s(x, t) = \Phi_s(x, t) - \Phi_e(x, t) - U(c_{ss}(x, t)) - FR_f j_n(x, t), \quad (15)$$

$$c_{ss}(x, t) \triangleq c_s(x, R_p, t), \quad (16)$$

for each t and x , where R_f is the film resistance of the solid-electrolyte interphase (SEI).

The *Butler-Volmer* equation describing the relationship between $j_n(x, t)$ and $\eta_s(x, t)$ [18], [16] is given by

$$j_n(x, t) = \frac{i_0(x, t)}{F} \left[\exp\left(\frac{\alpha_a F}{RT} \eta_s(x, t)\right) - \exp\left(\frac{-\alpha_c F}{RT} \eta_s(x, t)\right) \right], \quad (17)$$

where α_a and α_c are transport coefficients, and i_0 is the exchange current density. Note that (17) for the molar flux j_n is algebraic. Equation (17) can be understood as

follows. The current Fj_n corresponding to the molar flux of lithium ions exiting the solid particle can be expressed as $Fj_n = i_{\text{out}} - i_{\text{in}}$, where i_{out} and i_{in} depend on the overpotential η_s as

$$i_{\text{out}} = i_0 \exp\left(\frac{\alpha_a F}{RT} \eta_s\right), \quad i_{\text{in}} = i_0 \exp\left(\frac{-\alpha_c F}{RT} \eta_s\right).$$

The exchange current density i_0 in (17) is given by

$$i_0(x, t) = r_{\text{eff}} c_e(x, t)^{\alpha_a} \times (c_{s, \text{max}} - c_{ss}(x, t))^{\alpha_c} c_{ss}(x, t)^{\alpha_c}, \quad (18)$$

where r_{eff} is a constant, and $c_{s, \text{max}}$ is the maximum possible concentration of lithium in the solid particles of the electrode based on material properties. Thus, the term i_0 tends to zero as c_{ss} tends to either zero or $c_{s, \text{max}}$, or c_e tends to zero.

In summary, the equations that need to be solved are (2)–(4), (10), (14), and (17) with applied current I as the input, and the output given by the voltage V as defined in (1). Thus, the battery model is a system of nonlinear partial differential algebraic equations.

CONTROL AND ESTIMATION CHALLENGES FOR LI-ION BATTERIES

For automotive applications, a BMS is expected to predict the maximum available power and energy; safely charge and discharge the battery to meet regenerative braking and load-bearing requirements; track relevant parameters of the battery pack as it ages; and update the BMS to meet the desired performance criteria throughout its life. "Aging" includes effects of both chronological age and cycling [4], [5].

Prediction of the maximum available energy and power is required by the electronic control unit (ECU) to compute the vehicle's all-battery range in miles, as well as the power it can deliver to accelerate, if demanded. For various applications it is desirable to charge or discharge the battery as quickly as possible. However, fast charging or discharging can dangerously stress the electrodes of the battery as the lithium ions move in and out of the insertion sites. Such fast movement has several possible deteriorating effects. First, it stresses the lattice structure of the electrodes, potentially causing the lattice to disorder or even fracture.

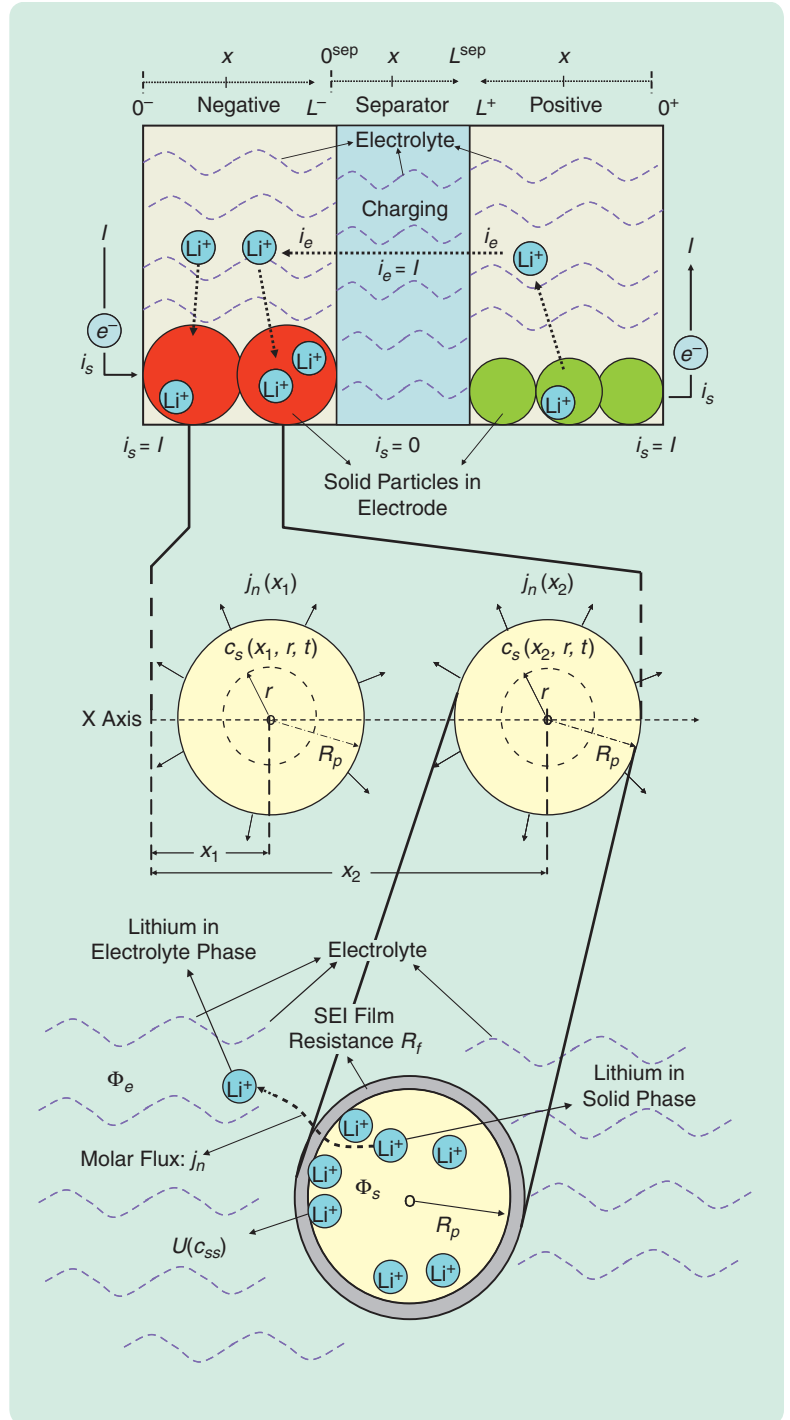


FIGURE 4 Schematic illustrating molar flux $j_n(x)$, and associated transition of lithium from solid phase to electrolyte phase in the electrode domains. For the reaction corresponding to solid-phase intercalation of lithium, the overpotential η_s represents the difference between the equilibrium thermodynamic potential difference at the existing surface concentration and the potential difference that a charged species would go through as it passes through the solid-electrolyte interphase (SEI) between the solid electrode and the electrolyte. Note that the electric potential in the particle is $\Phi_s(x)$, and the electric potential in the electrolyte is $\Phi_e(x)$. Furthermore, the thermodynamic potential difference at the existing surface concentration is given by $U(c_{ss}(x, t))$, where $U(\cdot)$ represents the open-circuit potential of the intercalation reaction, and $c_{ss}(x, t) \triangleq c_s(x, R_p, t)$ is the surface concentration of lithium in the solid particle. Additional potential drop at the SEI is due to the film resistance R_f .

Utilization and State of Charge

The local utilization at each point in the electrode is the ratio of the concentration of lithium in the solid electrode to its maximum possible concentration at that point. Thus, if $c(x, r)$ is the concentration at the point x and radius r in the spherical particle, and c_{\max} is the maximum possible concentration in the solid electrode, then the utilization at (x, r) is defined as $c(x, r) / c_{\max}$. The average utilization of the entire electrode is called the bulk state of charge (SOC) of the electrode. Note that SOC, which is a non-dimensional quantity, measures the charge contained in the electrode calculated in terms of the lithium concentration. Since the amount of lithium stored in the electrodes is related to the amount of charge available, SOC can be used as an indicator of available energy in the cell for a prescribed discharge rate.

Although the surface SOC, that is, the utilization at the surface of the solid particle, is directly related to the instantaneous available power, the bulk SOC is sometimes used to predict the available power. The reason for using bulk SOC, in contrast to surface SOC, is because bulk SOC can be determined by accurate current measurements. Given initial values, the bulk SOC can be computed from the current (assumed positive for charging) as

$$\text{SOC}^+(t) \triangleq \frac{3}{L^+(R_p^+)^3} \int_0^{L^+} \int_0^{R_p^+} r^2 \frac{c^+(x, r, t)}{c_{\max}^+} dr dx$$

This disorder or fracture might result in power and capacity loss, thereby accelerating aging of the battery. Second, since the fast movement of ions is accompanied by large potential drops across the battery, these drops induce side reactions that change the amount of available lithium and produce components that may reduce the performance and safety of the battery. Also, since the capacity of the battery is related to the quantity of lithium cycled between the electrodes, changes in the total available lithium might cause further loss of capacity.

Finally, as the battery ages, we need to track parameters that quantify aging of the battery pack. These changes are reflected in the BMS for power and energy prediction throughout the life of the battery pack. Additionally, this information can be used by the ECU to identify modules in the battery pack that need replacement. Each of these tasks reflects an estimation or control problem.

Power and Energy Prediction

Power and energy prediction demands a sufficiently accurate model that predicts voltage as a function of the input current. Furthermore, knowledge of the bulk *state of charge* (SOC) of the battery pack is often used by BMS algorithms to estimate energy stored in the pack. The bulk SOC of a cell is roughly the average utilization of either the positive or negative electrode, where utilization is the ratio of actual lithium concentration to the maximum possible concentration in the solid particles of the electrode;

$$\begin{aligned} &= \text{SOC}^+(t_0) - \int_{t_0}^t \frac{I(\tau)}{q \text{cap}^+} d\tau, \\ \text{SOC}^-(t) &\triangleq \frac{3}{L^-(R_p^-)^3} \int_0^{L^-} \int_0^{R_p^-} r^2 \frac{c^-(x, r, t)}{c_{\max}^-} dr dx \\ &= \text{SOC}^-(t_0) + \int_{t_0}^t \frac{I(\tau)}{q \text{cap}^-} d\tau, \end{aligned}$$

for the positive and negative electrode, respectively, where cap^+ and cap^- denote the corresponding theoretical capacities of the two electrodes, respectively. $\text{SOC}^+(t)$ and $\text{SOC}^-(t)$ are related, and hence, it suffices to use only $\text{SOC}^-(t)$ to represent the SOC of the battery. In applications, cap^+ and cap^- are typically chosen to be *nominal* capacities. These nominal capacities are measured experimentally by charging or discharging the cell between predefined voltage limits at a prescribed current rate. Thus, these nominal capacities do not correspond to the true theoretical capacities of the respective electrodes. Hence, SOC computed using nominal capacities might not represent the true bulk SOC, which is based on theoretical capacities of the individual electrodes.

see “Utilization and State of Charge.” The bulk SOC tells us how much charge in the form of lithium is available in the battery for discharge, thus yielding the energy content of the battery for a prescribed discharge rate.

Two quantities are of interest for predicting power output. *Instantaneous* power output of a battery is directly proportional to its instantaneous output voltage, where the output voltage of the battery is a function of the surface SOC. Thus, instantaneous power depends strongly on the surface SOC through the OCP of the cell [21], [22]. In addition to instantaneous power, *pulse* power is also relevant to automotive applications. *Pulse* power is defined as the maximum average power that can be delivered for a specified time period (usually 2–10 s) [23]. Like instantaneous power, pulse power depends on the knowledge of the surface SOC, in addition to the bulk SOC, as the battery is discharged.

Neither surface nor bulk SOC can be directly measured in a battery. In practical applications, the bulk SOC is often tracked by means of current integration, assuming precise current measurements and correct initial conditions are available; see “Utilization and State of Charge.” Since both surface and bulk SOC are defined in terms of the lithium concentration in the electrode, these immeasurable quantities can be computed from the states of the electrochemical model (2)–(4), (10), (14), and (17). Thus, both surface and bulk SOC can be tracked by observing the states of the electrochemical model; see the state estimator block in Figure 5. In

contrast, note that an equivalent circuit model has only bulk SOC as a state of the model, and not surface SOC. This lack of surface SOC information can result in reduced accuracy of power and energy prediction compared to an electrochemical model. Predicting power and energy and identifying feasible load currents based on demand and state of battery can be posed as an optimal control problem.

Safe Charging and Discharging

In a conventional BMS, safe charging and discharging of the battery pack is often realized by applying voltage and current limits on the operation of the cell. By imposing *constant* voltage bounds V_{lo} and V_{hi} , a cell can be charged or discharged as long as

$$V_{lo} \leq V(t) \leq V_{hi}, \quad (19)$$

for all time t . While these constant bounds might limit electric potentials within the electrodes from reaching unsafe values during operation, they are conservative, especially at high currents, where it is possible for the cell voltage to reach the voltage bounds in (19) even though the electrodes are far from potentially dangerous operation. Thus, the constant voltage-bound restriction can unnecessarily limit performance of the battery pack [21]. Additionally, these bounds may not guarantee safety as the battery ages and its characteristics change.

Since overpotentials determine the rate of a reaction, a strategy that guarantees safety during charge/discharge is to track overpotentials of reactions that can damage the cell. In a Li-ion battery, reactions that occur in addition to the primary reaction of intercalation of lithium in the electrode are called *side reactions*. One side reaction, which is relevant for avoiding damage to the cell during charging or discharging, is the side reaction that consumes or releases lithium and thus changes the capacity of the cell. An example of such a side reaction that can create a potential safety hazard is the side reaction of lithium plating on the surface of the electrodes [24]. Though additional constraints might have to be satisfied to guarantee safe operation of the battery pack, we focus on this side-reaction overpotential for illustration.

As described in "Overpotential of a Reaction," the overpotential for a side reaction in a Li-ion battery can be described as

$$\eta_{sr} = \Phi_s - \Phi_e - U_{sr}(c_{ss}) - R_{f, sr} j_{n_{sr}}, \quad (20)$$

where sr denotes quantities corresponding to the side reaction. The term U_{sr} denotes the equilibrium potential of the side reaction and is assumed to be known. Since $j_{n_{sr}} \approx 0$, the term $R_{f, sr} j_{n_{sr}}$ can be assumed negligible. Thus, it usually suffices to know Φ_s , Φ_e , and c_{ss} in order to compute overpotentials of side reactions. For the side reaction of lithium plating, U_{sr} is zero [24], and hence the overpotential is

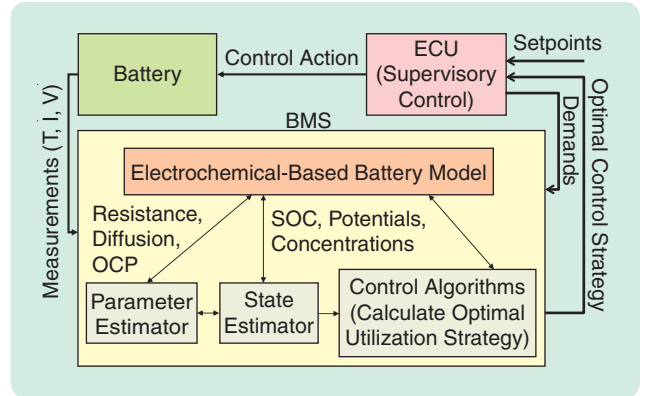


FIGURE 5 Architecture of an advanced battery management system (BMS). Unlike a standard BMS, an advanced BMS uses a physics-based electrochemical model instead of an ad hoc equivalent circuit model. In addition, the BMS has three blocks corresponding to parameter estimation, state estimation, and control algorithms for optimal utilization of the battery. The parameter and state estimator together guarantee that the electrochemical model is sufficiently accurate over its entire operational lifetime. The control algorithms block uses the model information to compute the optimal charging and discharging profile for the battery based on the desired reference input from the electronic control unit.

$$\eta_{sr}(x, t) = \Phi_s(x, t) - \Phi_e(x, t). \quad (21)$$

Since Φ_s and Φ_e are state variables of the electrochemical model, we can observe the states at all times during operation to compute the overpotentials. As long as the overpotentials do not violate certain limits, it is safe to charge or discharge the cell. As an example, to minimize the reaction rate of lithium plating during charging, we need to constrain η_{sr} in the negative electrode such that, for all x and t ,

$$\eta_{sr}(x, t) > 0. \quad (22)$$

Similarly, if further side reactions need to be considered, then additional constraints on η_{sr} arise for each side reaction.

Figure 6 compares two strategies for charging a fresh cell starting from 2.9 V. The plots show the behavior of the output voltage and overpotentials for a constant charging current at approximately 1.5 C (see "C Rate of a Current"). In the first strategy based on (19), charging is stopped when the voltage limit of $V_{hi} = 4.2$ V is reached, yielding a charge capacity of 2.897 ampere-hours (A-h). In the second strategy, the same cell is charged as long as η_{sr} satisfies (22) everywhere in the cell. As shown in Figure 6, the cell can be charged to the higher capacity of 3.09 A-h, yielding 6.7% extra charge capacity, while the final voltage is 4.274 V. Thus, since charging is stopped even though the overpotential η_{sr} is above 11 mV, the voltage constraint (19) is conservative, and hence it is safe to charge further.

On a similar note, as the cell ages, the constraint (19) may change from being conservative to being potentially

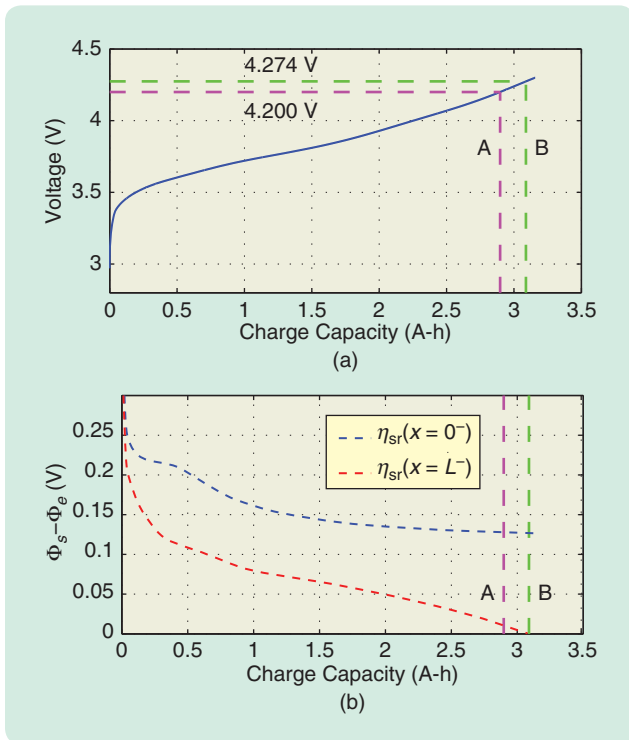


FIGURE 6 Comparison of charging strategies. (a) Shows the voltage of the cell as it is charged, whereas (b) shows the side reaction overpotential $\eta_{sr} = \Phi_s - \Phi_e$ corresponding to lithium plating in the negative electrode. In the first strategy marked by “A,” the charging is stopped when the voltage hits 4.2 V, yielding a charge capacity of 2.897 A-h. In (b), $\eta_{sr} \geq 11$ mV everywhere in the electrode, and hence further charging is possible. In the second strategy, marked by “B,” the same cell is charged until $\eta_{sr} = \Phi_s - \Phi_e = 0$ somewhere in the cell. The side reaction overpotential in (b) reaches zero first at the separator shown by $\eta_{sr}(x = L^-)$. Thus, we can charge to a higher capacity of 3.09 A-h yielding 6.7% extra charge capacity using strategy “B.”

unsafe due to age-induced behavior changes. One example of an age-induced behavior change is an unfavorable change in the capacity ratio of the individual electrodes [25] or a decrease in the diffusion coefficient in the negative electrode with age. Then, for the aged cell, while the voltage is less than V_{hi} in (19), the overpotential η_{sr} can be dangerously low. Figure 7 compares the strategies for charging an aged cell starting from 2.9 V. In the first strategy based on (19), charging is stopped when the voltage limit of $V_{hi} = 4.2$ V is reached. In the second strategy, the same cell is charged so that $\eta_{sr} = \Phi_s - \Phi_e$ satisfies (22). Figure 7 shows that, in the first strategy, η_{sr} is negative for the last portion of charging between 2.872 A-h and 3.133 A-h, or between 4.11 V and 4.2 V. During this period, the cell can suffer damage, reducing its performance or even exposing it to a higher risk of explosion.

Note that using strategy “B” allows for aggressive charging, while protecting the battery from damage. Additionally, strategy “B” allows for a less conservative design and hence less expensive batteries. Since the overpotential

C Rate of a Current

The C rate of a current (charging or discharging) is defined as the ratio of the current in amperes (A) to the nominal capacity C_{nom} of the cell in ampere-hours (A-h). Thus, if the nominal capacity of a cell is 3 A-h, then a 1 C, C/2, and 2 C current correspond to currents of magnitude 3 A, 1.5 A, and 6 A, respectively. Note that the C rate has a dimension of [A]/[A-h] = 1/h. The notation C/2 is typically used in place of 0.5 C.

The C rate of a current indicates the magnitude of the current relative to the size of the battery. This relative magnitude of the current governs various electrochemical effects, and thus the C rate allows for a quick comparison of the behavior of the battery for input currents, irrespective of the size of the battery.

η_{sr} is a function of states, estimating η_{sr} is an observer design problem. Furthermore, utilizing model and state information for optimal charging and discharging is a control problem, as indicated by the control algorithms block in Figure 5.

Parameter Estimation

As the battery pack ages, its physical characteristics, such as film resistance, diffusion coefficients, and other electrochemical model parameters, change. To predict power and energy, as well as to track aging of the battery, we need to track the parameters of the electrochemical model, as indicated by the parameter estimator block in Figure 5. However, not all parameters have to be tracked, since some have negligible effect, while others do not vary significantly with age. Unlike an equivalent circuit model, these electrochemical model parameters have a physical interpretation and thus are directly correlated with aging of the pack. Knowledge of these cell parameters can also be used to determine whether any cell of the battery pack needs replacement.

FRAMEWORK FOR THE LI-ION BATTERY MODEL

In this section, we reformulate the Li-ion battery model to facilitate computation. This reformulation is exact but can also be used to construct various approximations to the electrochemical model.

Notational Background

Let $\mathcal{C}^r(a, b)$ denote the set of real-valued, r -times continuously differentiable functions with domain $(a, b) \in \mathbb{R}$. Thus, $\mathcal{C}^0(a, b)$ represents the set of functions that are continuous. By abuse of notation, $\mathcal{C}^{-1}(a, b)$ denotes the set of discontinuous functions whose integrals exist and are continuous. More precisely, this function space is a subset of the Sobolev space $\mathcal{H}^1(\mathbb{R})$ [26]. Thus, whereas piecewise-continuous functions belongs to $\mathcal{C}^{-1}(\mathbb{R})$, an impulse

function, usually described as the derivative of the Heaviside step function, does not belong to $\mathcal{C}^{-1}(\mathbb{R})$ since its integral is discontinuous. Note that $\mathcal{C}^\omega(\mathbb{R}) \subset \mathcal{C}^\infty(\mathbb{R}) \subset \dots \subset \mathcal{C}^0(\mathbb{R}) \subset \mathcal{C}^{-1}(\mathbb{R})$, where $\mathcal{C}^\omega(\mathbb{R})$ represents the space of analytic functions.

A function map \mathcal{F} takes an element of $\mathcal{C}^r(a, b)$ to $\mathcal{C}^q(a, b)$, where r and q are integers. We write $\mathcal{F}: \mathcal{C}^r(a, b) \rightarrow \mathcal{C}^q(a, b)$. Also, $\mathcal{F}(g)^\circ(a)$ denotes the evaluation of the function map, applied to a function g , at $a \in \mathbb{R}$. For example, consider the function map given by the differential operator $\mathbf{D}: \mathcal{C}^r(a, b) \rightarrow \mathcal{C}^{r-1}(a, b)$, where r is a positive integer. Since $\mathbf{D}(\sin) = \cos$, we have $\mathbf{D}(\sin)^\circ(a) = (\cos)^\circ(a) = \cos(a)$.

Next, let $g: \mathbb{R} \times \mathbb{R} \rightarrow \mathbb{R}$. Then, the t -restriction of g is defined as $g^t(x) \triangleq g(x, t)$. Hence, $g^t: \mathbb{R} \rightarrow \mathbb{R}$ denotes the value of g for each fixed t . For example, if $c_e(x, t)$ denotes the concentration of electrolyte at x at time t , then $c_e^t(x)$ is the concentration profile in space at time t . Hence, $c_e^t(x)$ denotes a snapshot of the concentration profile. In a similar fashion, the x -restriction $c_e^x(t)$ of $c_e(x, t)$ denotes the time evolution of the concentration at each x . Furthermore, if $h: \mathbb{R} \rightarrow \mathbb{R}$, then h^t is the scalar given by $h^t = h(t) \in \mathbb{R}$.

Reformulation of the PDE System

We begin by reducing the system of five PDEs (2)–(4), (10), (14), and one algebraic equation (17) to two PDEs with time derivatives and algebraic equations. We focus on either the positive or negative electrode for this purpose. The spatial domain is assumed to run from 0 to L . Thus, for the negative and positive electrode, the corresponding domains are $[0^-, L^-]$ and $[0^+, L^+]$, respectively (see Figure 2). The key idea is to solve the PDEs explicitly in the spatial variable as function maps. Furthermore, we assume throughout this analysis that the input current $I(t)$ is such that solutions to the battery model given by (2)–(4), (10), (14), and (17) exist and belong to $\mathcal{C}^{-1}[0, L] \times \mathcal{C}^{-1}[0, L]$ for each time t and each spatial domain discussed above.

PDE in Spatial Variables

Consider (14). Given $I(t) \in \mathbb{R}$, we have $j_n^t(x) \in \mathcal{C}^q[0, L]$ for each time $t \in \mathbb{R}$, where the integer $q \geq -1$. Note that $I^t = I(t)$ is a scalar for each $t \in \mathbb{R}$. Now, we can solve (14) as

$$i_e(x, t) = \int_0^x aFj_n(\xi, t)d\xi + i_{e_0}(I(t)),$$

or, equivalently, as

$$i_e^t(x) = \int_0^x aFj_n^t(\xi)d\xi + i_{e_0}(I^t),$$

where $i_{e_0}(\cdot)$ is an integration constant independent of x , which is fixed based on the boundary condition. Note that i_{e_0} is a function of t through $I(t)$. Define the function map $\mathcal{F}_{i_e}: \mathcal{C}^q[0, L] \times \mathbb{R} \rightarrow \mathcal{C}^{q+1}[0, L]$ as

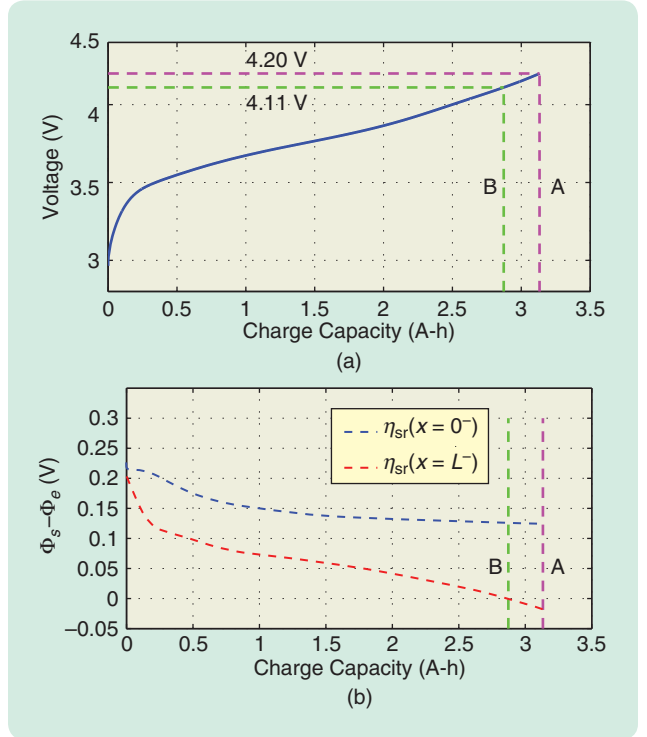


FIGURE 7 Comparison of charging strategies applied to an aged cell. Part (a) shows the voltage of the cell as it is charged, whereas (b) shows the side reaction overpotential $\eta_{sr} = \Phi_s - \Phi_e$ corresponding to lithium plating in the negative electrode. As in Figure 6, in the first strategy marked by “A,” charging is stopped when the voltage reaches 4.2 V. In (b), the overpotential is negative for the last portion of charging between 2.872 A-h and 3.133 A-h, or between 4.11 V and 4.2 V. Thus, strategy “A” overcharges the cell, which damages it and may increase the risk of explosion. Compared to “A,” strategy “B” stops charging at 4.11 V, where the overpotential $\eta_{sr} = \Phi_s - \Phi_e$ at the separator [shown by $\eta_{sr}(x = L^-)$ in (b)] reaches zero since it is dangerous to continue charging.

$$\mathcal{F}_{i_e}(g, \zeta)^\circ(x) \triangleq \int_0^x aFg(\xi)d\xi + i_{e_0}(\zeta). \quad (23)$$

Then it follows that a solution of the PDE in (14) for each t is

$$i_e(x, t) = i_e^t(x) = \mathcal{F}_{i_e}(j_n^t, I^t)^\circ(x). \quad (24)$$

Intuitively, (24) means that there exists an operator \mathcal{F}_{i_e} such that, if we input the function j_n^t along with the value of the current $I(t)$ for some time t into \mathcal{F}_{i_e} , then the output i_e^t is the spatial profile of ionic current density in the electrolyte at time t . Thus, if j_n is known, i_e can be computed explicitly.

Since the boundary condition of the PDE is known, we absorb the constant of integration in \mathcal{F}_{i_e} . Indeed, the constant of integration is obtained by setting i_e to either zero or $\pm I(t)$ at one of the boundaries ($x = 0$ or $x = L$) of the domain. Note that two boundary conditions must be satisfied since the value of $i_e^t(x)$ is known at both $x = 0$ and $x = L$. Depending on whether we consider the positive or

negative electrode, or the separator, the boundary conditions are given by

$$\{i_e^t(0), i_e^t(L)\} = \begin{cases} \{0, I(t)\} / \{0, -I(t)\} & \text{(for negative/positive electrode),} \\ \{I(t), -I(t)\} & \text{(for separator).} \end{cases} \quad (25)$$

Since the PDE (14) is a first-order PDE, and thus requires only one boundary condition, we obtain an overconstrained problem. However, it turns out that the additional boundary condition becomes a boundary condition for (2) through the variable j_n in the Butler-Volmer kinetics given by (17). For now, we choose one of the boundary conditions (at either $x=0$ or $x=L$) to determine i_{e_0} in (23).

Next, we solve for the PDE (2) in a similar fashion as

$$\Phi_s(x, t) = \Phi_s^t(x) = \mathcal{F}_{\Phi_s}(j_n^t, I^t)^\circ(x) + \phi_{s_0}(t), \quad (26)$$

where $\mathcal{F}_{\Phi_s} : \mathcal{C}^q[0, L] \times \mathbb{R} \rightarrow \mathcal{C}^{q+2}[0, L]$ is defined as

$$\mathcal{F}_{\Phi_s}(g, \zeta)^\circ(x) \triangleq \frac{1}{\sigma_0} \int_0^x (F_i(g, \zeta)^\circ(w) - \zeta) dw, \quad (27)$$

and $\phi_{s_0}(t)$ is an integration constant. Note that, unlike \mathcal{F}_{i_e} in (23), we do not absorb the integration constant in \mathcal{F}_{Φ_s} . This structure is chosen because we do not know the boundary condition a priori, and thus, $\phi_{s_0}(t)$ is an unknown to be determined.

Similarly, assuming a constant t_+^0 , and performing some manipulations, we can solve for the PDE in (3) for each time t as

$$\Phi_e(x, t) = \Phi_e^t(x) = \mathcal{F}_{\Phi_e}(j_n^t, c_e^t, I^t)^\circ(x), \quad (28)$$

where $\mathcal{F}_{\Phi_e} : \mathcal{C}^q[0, L] \times \mathcal{C}^{q+1}[0, L] \times \mathbb{R} \rightarrow \mathcal{C}^{q+2}[0, L]$ is

$$\mathcal{F}_{\Phi_e}(g, h, \zeta)^\circ(x) \triangleq \int_0^x \frac{-F_i(g, \zeta)^\circ(w)}{\kappa(h(w))} dw + \frac{2RT}{F} (1 - t_c^0) \ln(f_{c/a} h(x)) + \phi_{e_0}(g, h, \zeta), \quad (29)$$

and $f_{c/a}$ is a known function of h . In this case, since the boundary condition for this PDE is known, we absorb the constant of integration in the definition of \mathcal{F}_{Φ_e} . This constant of integration is obtained by equating Φ_e to zero at the current collector in the positive electrode. Thus, $\mathcal{F}_{\Phi_e}(j_n^t, c_e^t, I^t)^\circ(0^+) = 0$. Note that the constant of integration ϕ_{e_0} depends on whether the domain under consideration is the positive or negative electrode, or the separator.

Summarizing, (24), (26), and (28) imply that if $j_n(x, t)$, $c_e(x, t)$ and $I(t)$ are given, then we obtain $\Phi_s(x, t)$, $\Phi_e(x, t)$,

and $i_e(x, t)$ (and hence $i_s(x, t)$ since $i_s(x, t) + i_e(x, t) = I(t)$ for all $(x, t) \in [0, L] \times \mathbb{R}$).

Butler-Volmer Kinetics

We now derive the expressions determining the remaining unknowns, namely, $j_n(x, t)$ and $\phi_{s_0}(t)$. Consider (15) and (17). Substituting for Φ_s and Φ_e from (27) and (29), respectively, in (15) yields

$$\eta_s(x, t) = \mathcal{F}_{\Phi_s}(j_n^t, I^t)^\circ(x) + \phi_{s_0}^t - \mathcal{F}_{\Phi_e}(j_n^t, c_e^t, I^t)^\circ(x) - U(c_{ss}^t(x)) - R_f j_n^t(x) F. \quad (30)$$

Equation (30) suggests that we can express η_s as a function of j_n , c_e , c_{ss} , I , and ϕ_{s_0} for every x and t . Note that $\phi_{s_0}^t = \phi_{s_0}(t)$ in (30) is the unknown boundary condition, described as the constant of integration in (26). Similarly, the exchange current density can be expressed as a function of c_e and c_{ss} from (18). Therefore, the Butler-Volmer kinetics in (17) can be expressed as

$$j_n(x, t) = j_n^t(x) = \mathcal{F}_{j_n}(j_n^t, c_e^t, c_{ss}^t, I^t, \phi_{s_0}^t)^\circ(x), \quad (31)$$

where $\mathcal{F}_{j_n} : \mathcal{C}^q[0, L] \times \mathcal{C}^{q+1}[0, L] \times \mathcal{C}^{q+1}[0, L] \times \mathbb{R} \times \mathbb{R} \rightarrow \mathcal{C}^q[0, L]$ is

$$\mathcal{F}_{j_n}(f, g, h, \zeta, \beta)^\circ(x) \triangleq \frac{i_0(x)}{F} \left[\exp\left(\frac{\alpha_a F}{RT} \eta_s(x)\right) - \exp\left(\frac{-\alpha_c F}{RT} \eta_s(x)\right) \right], \quad (32)$$

$$i_0(x) \triangleq r_{\text{eff}}(g(x))^{\alpha_c} (c_{s, \text{max}} - h(x))^{\alpha_a} (h(x))^{\alpha_c}, \quad (33)$$

$$\eta_s(x) \triangleq \mathcal{F}_{\Phi_s}(f, \zeta)^\circ(x) - \mathcal{F}_{\Phi_e}(f, g, \zeta)^\circ(x) - U(h(x)) - R_f f(x) F + \beta. \quad (34)$$

The algebraic equation (31) must be satisfied for every x and time t . Given the electrolyte concentration $c_e^t(x)$, the surface concentration of the solid particle $c_{ss}^t(x) = c_s(x, R_p, t)$, and the current I^t , we need to find $j_n^t(x)$ and $\phi_{s_0}^t$ that satisfy (31). However, there are two unknowns $j_n(x, t)$ and $\phi_{s_0}(t)$, and only one equation, specifically, (31). To solve for j_n and ϕ_{s_0} together, we use the additional boundary condition on i_e . In the derivation of \mathcal{F}_{i_e} in (23), we use the boundary condition $i_e(0, t) = 0$. Since i_e also satisfies $i_e(L, t) = I(t)$ at the separator-electrode interface, substituting the boundary condition $i_e(L, t) = I(t)$ into (24) yields

$$i_e(L, t) = i_e^t(L) = \mathcal{F}_{i_e}(j_n^t, I^t)^\circ(L) = I(t), \quad (35)$$

which is an algebraic constraint on $j_n(\cdot, t)$. Then, for a given electrolyte concentration $c_e(x, t)$, surface concentration of the electrode $c_{ss}(x, t)$, and current $I(t)$, (31) and (35) are solved together to obtain the molar flux $j_n(x, t)$ and the boundary condition on Φ_s given by $\phi_{s_0}(t)$. Thus,

the solutions of the full Li-ion battery model given by (2)–(4), (10), (14), and (17) are equivalent to the solutions of (4) and (10) involving dynamics in time, while satisfying additional algebraic constraints in space given by (31) and (35) at all times t .

The above analysis shows that the Li-ion battery model (2)–(4), (10), (14), and (17) can be described by the two diffusion equations (4) and (10), which capture the transport of lithium in the electrolyte phase and solid phase, respectively. The flux j_n , which acts as the source and boundary condition for (4) and (10), respectively, is obtained by solving the algebraic equations (31) and (35).

SIMPLE APPROXIMATION OF THE REFORMULATED MODEL

Numerical techniques for solving (2)–(4), (10), (14), and (17) involve discretizing the spatial domain to yield a system of differential algebraic equations (DAEs). The algebraic equations of the DAE are equivalent to the algebraic equations obtained by discretizing (31) and (35). However, these equations are difficult to solve analytically without additional simplifying assumptions. We thus consider the special case where no spatial variations are allowed. We use the reformulated Li-ion battery model (4), (10), (31), and (35) and demonstrate the generality of this form by deriving an approximate model [19], [20], [27]. We use the coarsest possible discretization for the spatial variable x in (4), (10), (31), and (35), specifically, one node for the positive and negative electrode each, and one node for the separator.

This simplification yields the approximate model known as the single particle model (SPM) [19], [20], [27].

Assumptions Involving the Approximation

The SPM is illustrated in Figure 8, where quantities at the nodes represent averages over the entire domain. Furthermore, we assume that $\partial c_e / \partial x \approx 0$ and $\partial c_e / \partial t \approx 0$. This approximation holds if I is small or κ is large. Then $c_e(x, t) \equiv c_e^0$. Also, (4) implies $i_e(x, t) = i_e^0(t)$, which implies that, within each domain (positive electrode, negative electrode, or separator), i_e remains constant with respect to x . Then we can express i_e for the entire electrode by one value in each spatial domain of the cell.

Solution for the Single Particle Model

Since each domain is represented by only one node, we express the corresponding variables in the positive electrode as scalar functions of time denoted as $j_n^+(t)$, $i_e^+(t)$, $\Phi_s^+(t)$, $\Phi_e^+(t)$, $c_e^+(t)$, $c_s^+(r, t)$, and similarly for the negative electrode, as shown in Figure 8. In this case, the function maps can be directly solved for the reformulated model (4), (10), (31), and (35). From (23) and (24), we obtain

$$\begin{aligned} 0 &= i_e(0^+, t) = i_e^+(t) = \mathcal{F}_{i_e}(j_n^+, I^+) \circ (0^+) \\ &= \int_{0^+}^0 a^+ F j_n^{+,t} d\xi + i_{e_0}(I^+) = i_{e_0}(I^+). \end{aligned}$$

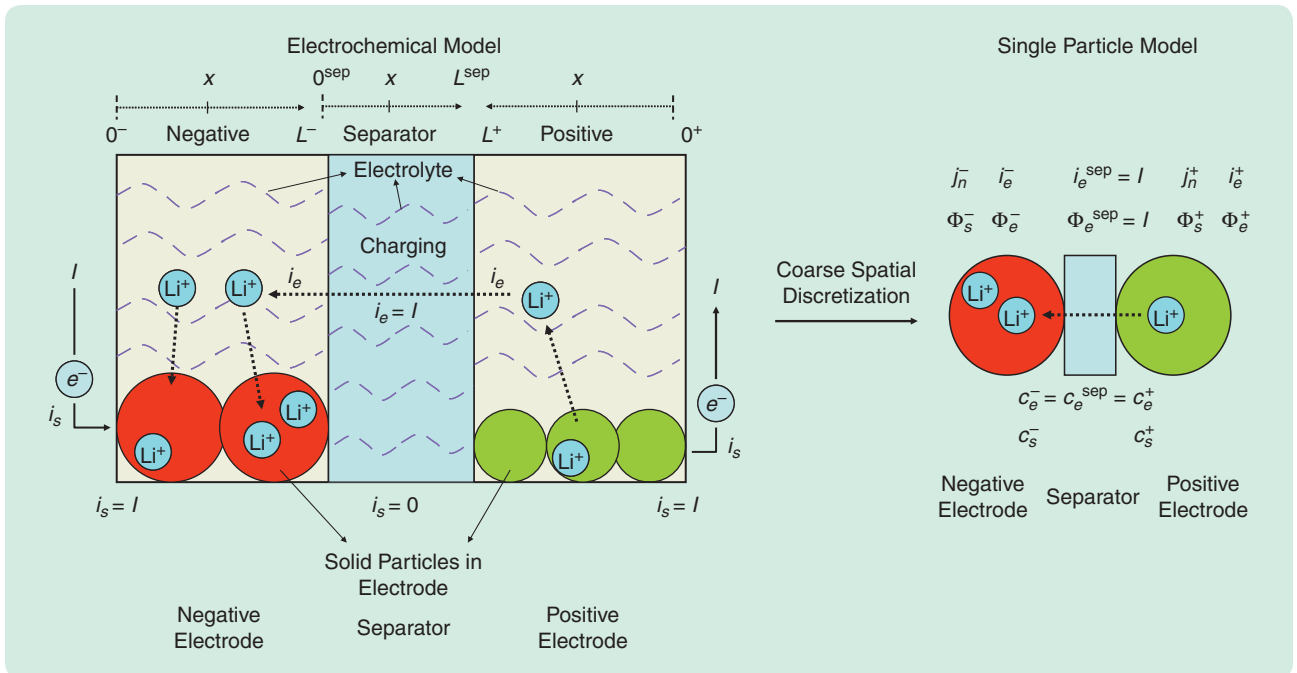


FIGURE 8 Single particle model. Since only one node is chosen in the electrode, there is only one solid spherical particle. Furthermore, we can consider the value at each node to be an averaged quantity over the electrode. This simplification holds only for small currents or for an electrolyte with a high ionic conductance.

Thus, $i_{e_0}(I^t) = 0$ is obtained from the boundary condition $i_e(0^+, t) = i_e^+(t) = 0$. Next, substituting this boundary condition in \mathcal{F}_{i_e} , and solving (35) implies that

$$\begin{aligned} -I(t) &= i_e^{\text{sep}}(t) = i_e(L^+, t) = \mathcal{F}_{i_e}(j_n^t, I^t) \circ (L^+) \\ &= \int_{0^+}^{L^+} a^+ F j_n^{+,t} d\xi = j_n^{+,t} L^+ a^+ F, \end{aligned}$$

where $i_e^{\text{sep}}(t)$ is the current in the separator and hence,

$$j_n^+(t) = j_n^{+,t} = -\frac{I(t)}{Fa^+L^+}. \quad (36)$$

Continuing in the above fashion, it follows from (26) and (27), that

$$\Phi_s^+(t) = \frac{1}{\sigma} \int_{0^+}^{0^+} (i_e^+(t) - I(t)) dw + \phi_{1_0}^+(t) = \phi_{1_0}^+(t). \quad (37)$$

Similarly, since $\phi_{e_0}^+(t) = 0$ from the boundary condition $\Phi_e = 0$ at the current collector of the positive electrode, it follows that $\Phi_e^+(t) = 0$. Finally, we apply the last algebraic constraint (31) to (36), and, choosing $\alpha_a = \alpha_c = 1/2$, it follows that

$$\frac{-I(t)}{2a^+L^+} = r_{\text{eff}} \sqrt{c_e^0 c_{ss}^+(t) (c_{s,\text{max}}^+ - c_{ss}^+(t))} \sinh(\eta^+), \quad (38)$$

$$\eta^+ = \frac{F}{2RT} \left(\phi_{1_0}^+(t) - U^+(c_{ss}^+(t)) + \frac{R_f^+ I(t)}{a^+L^+} \right), \quad (39)$$

where $U^+(\cdot)$ is the OCP of the positive electrode and is assumed known.

Similarly, for the negative electrode, we obtain

$$\begin{aligned} 0 &= i_e(0^-, t) = i_e^-(t) = \mathcal{F}_{i_e}(j_n^t, I^t) \circ (0^-) \\ &= \int_{0^-}^{0^-} a^- F j_n^{-,t} d\xi + i_{e_0}(I^t) = i_{e_0}(I^t). \end{aligned}$$

Thus, the boundary condition $i_e(0^-, t) = i_e^-(t) = 0$ implies $i_{e_0}(I(t)) = 0$. Substituting this boundary condition into \mathcal{F}_{i_e} and solving (35) implies

$$\begin{aligned} I(t) &= i_e^{\text{sep}}(t) = i_e(L^-, t) = \mathcal{F}_{i_e}(j_n^t, I^t) \circ (L^-) \\ &= \int_{0^-}^{L^-} a^- F j_n^{-,t} d\xi = j_n^{-,t} L^- a^- F, \end{aligned}$$

where $i_e^{\text{sep}}(t)$ is the current in the separator and hence,

$$j_n^-(t) = j_n^{-,t} = \frac{I(t)}{Fa^-L^-}. \quad (40)$$

Equations (26) and (27) imply that

$$\Phi_s^-(t) = \frac{1}{\sigma} \int_{0^-}^{0^-} (i_e^-(t) - I(t)) dw + \phi_{s_0}^-(t) = \phi_{s_0}^-(t). \quad (41)$$

Furthermore, (29) with the boundary condition $\Phi_e = 0$ at the current collector of the positive electrode yields $\phi_{e_0}^+(t) = 0$. Hence,

$$\Phi_e^-(t) = -\frac{1}{\kappa} \int_{0^+}^{0^-} i_e(x, t) dx,$$

where the limits of integration denote that the integration is from the positive current collector to the negative current collector. Following the assumption for the SPM that $I(t)$ is small, or the conductance κ is large, we obtain $|I(t)| / \kappa \ll 1$. Since $|i_e(x, t)| \leq |I(t)|$ in the cell, it follows that

$$\Phi_e^-(t) = -\frac{1}{\kappa} \int_{0^+}^{0^-} i_e(x, t) dx \approx 0, \quad (42)$$

Lastly, since $\alpha_a = \alpha_c = 1/2$, (31) yields

$$\frac{I(t)}{2a^-L^-} = r_{\text{eff}} \sqrt{c_e^0 c_{ss}^-(t) (c_{s,\text{max}}^- - c_{ss}^-(t))} \sinh(\eta^-), \quad (43)$$

$$\eta^- = \frac{F}{2RT} \left(\phi_{s_0}^-(t) - U^-(c_{ss}^-(t)) - \frac{R_f^- I(t)}{a^-L^-} \right), \quad (44)$$

where $U^-(\cdot)$ is the OCP of the negative electrode and is assumed known. We can solve (38) and (39) for $\phi_{s_0}^+(t)$, and (43) and (44) for $\phi_{s_0}^-(t)$, yielding $\Phi_s^+(t)$ from (37) and $\Phi_s^-(t)$ from (41). Note that $\Phi_s^+(t)$ and $\Phi_s^-(t)$ are equal to their boundary values $\phi_{s_0}^+(t)$ and $\phi_{s_0}^-(t)$, respectively. Also, we need to compute $c_{ss}^+(t) = c_s^+(R_p, t)$ and $c_{ss}^-(t) = c_s^-(R_p, t)$ by solving the PDE (4), where $j_n(x, t) = j_n^+(t)$ and $j_n(x, t) = j_n^-(t)$, respectively. Then, the output voltage $V(t) = \phi_{s_0}^+(t) - \phi_{s_0}^-(t)$.

Summary of the Approximate Model

Summarizing, the approximate model (SPM [19], [20], [27]) is given as follows. Let $I(t)$ be the input current to the battery. Then, the output voltage of the battery is computed as $V(t) = \phi_{s_0}^+(t) - \phi_{s_0}^-(t)$, where $\phi_{s_0}^+(t)$ and $\phi_{s_0}^-(t)$ are obtained by solving (43), (44), and (38), (39), respectively, and are given as

$$\begin{aligned} \phi_{s_0}^-(t) &= \frac{2RT}{F} \sinh^{-1} \left(\frac{I(t)}{2a^-L^- r_{\text{eff}} \sqrt{c_e^0 c_{ss}^-(t) (c_{s,\text{max}}^- - c_{ss}^-(t))}} \right) \\ &\quad + U^-(c_{ss}^-(t)) + \frac{R_f^- I(t)}{a^-L^-}, \end{aligned} \quad (45)$$

$$\begin{aligned} \phi_{s_0}^+(t) &= \frac{2RT}{F} \sinh^{-1} \left(\frac{I(t)}{2a^+L^+ r_{\text{eff}} \sqrt{c_e^0 c_{ss}^+(t) (c_{s,\text{max}}^+ - c_{ss}^+(t))}} \right) \\ &\quad + U^+(c_{ss}^+(t)) + \frac{R_f^+ I(t)}{a^+L^+}, \end{aligned} \quad (46)$$

where $c_{ss}^-(t) \triangleq c_s^-(R_p^-, t)$ and $c_{ss}^+(t) \triangleq c_s^+(R_p^+, t)$. The concentrations $c_s^-(R_p^-, t)$ and $c_s^+(R_p^+, t)$ are obtained by solving the PDEs

$$\frac{\partial c_s^-(r, t)}{\partial t} = \frac{1}{r^2} \frac{\partial}{\partial r} \left(D_s^- r^2 \frac{\partial c_s^-(r, t)}{\partial r} \right), \quad (47)$$

where the boundary and initial conditions are given by

$$\left. \frac{\partial c_s^-}{\partial r} \right|_{r=0} = 0, \quad (48)$$

$$\left. \frac{\partial c_s^-}{\partial r} \right|_{r=R_p^-} = -\frac{I(t)}{D_s^- Fa^- L^-}, \quad (49)$$

$$c_s^-(r, 0) = c_s^{0,-}(r), \quad (50)$$

and

$$\frac{\partial c_s^+(r, t)}{\partial t} = \frac{1}{r^2} \frac{\partial}{\partial r} \left(D_s^+ r^2 \frac{\partial c_s^+(r, t)}{\partial r} \right), \quad (51)$$

where boundary and initial conditions are given by

$$\left. \frac{\partial c_s^+}{\partial r} \right|_{r=0} = 0, \quad (52)$$

$$\left. \frac{\partial c_s^+}{\partial r} \right|_{r=R_p^+} = \frac{I(t)}{D_s^+ Fa^+ L^+}, \quad (53)$$

$$c_s^+(r, 0) = c_s^{0,+}(r). \quad (54)$$

The reformulated model (4), (10), (31), and (35) can also be used to approximate the electrochemical model using approaches such as proper orthogonal decomposition (POD) [28], spectral methods [22], and model reformulation methods [29].

EXPERIMENTAL AND SIMULATION RESULTS

We now compare the electrochemical model for Li-ion cells given by (4) and (10), along with the algebraic constraints (31) and (35), with experiments. We also present results that compare the SPM given by (45)–(47), and (51) with the same experimental data and also with the electrochemical model (4), (10), (31), and (35).

Various tests can be performed to obtain experimental data for validating a cell model. Some examples of these tests include constant-current charge and discharge at different C rates, hybrid pulse-power characterization (HPPC) [30], and various drive cycles. For validation purposes relevant to automotive applications, we present experimental results for a measured drive cycle of a hybrid electric vehicle. Experiments are carried out on a commercial 18650 Li-ion cell, where the input current to the cell is based on a HEV power profile measurement. For the experiments on the commercial 18650 Li-ion cell, all measurements are performed on an Arbin BT2000 battery tester.

To obtain the parameters of the cell model, we either directly measure the physical parameters, or fit them to data obtained from experiments. In this case, the OCPs of the individual materials are measured in half-cell experiments. The key parameters fitted to the 18650 cell are the individual

volume fractions and the total lithium content in the solid electrode. Of the remaining model parameters, most are either measured directly or adopted from the literature [24].

The current applied to the 18650 cell, as calculated from a measured power profile of an HEV driving aggressively in the city and on a German highway, is depicted in Figure 9. Also shown in Figure 9 is the bulk SOC swing computed for the applied current; see “Utilization and State of Charge” for more details on how to compute bulk SOC. The initial value of the bulk SOC is normalized to have a value of one at a rest voltage of 4.2 V, and the nominal capacity is defined as the capacity discharged between 4.2 V and 2.8 V quasi-statically. The nominal capacity is measured to be about 1.5 A-h.

The resulting output voltage from the electrochemical model and the SPM is shown in Figure 10, along with the experimental results. Figure 10(b) and (c) shows a zoomed-in version of Figure 10(a) for several time windows. As shown in Figure 10, the electrochemical model has a measured mean error of about 13 mV. Furthermore, as shown in Figure 10, the SPM captures the trends of the experimental data. However, the SPM has a mean error of 28 mV. Comparing the plots in Figure 10 with the plot for the applied input current in Figure 9(a), we see that the errors in the SPM occur for either large values of applied current or during relaxation after applying a current pulse

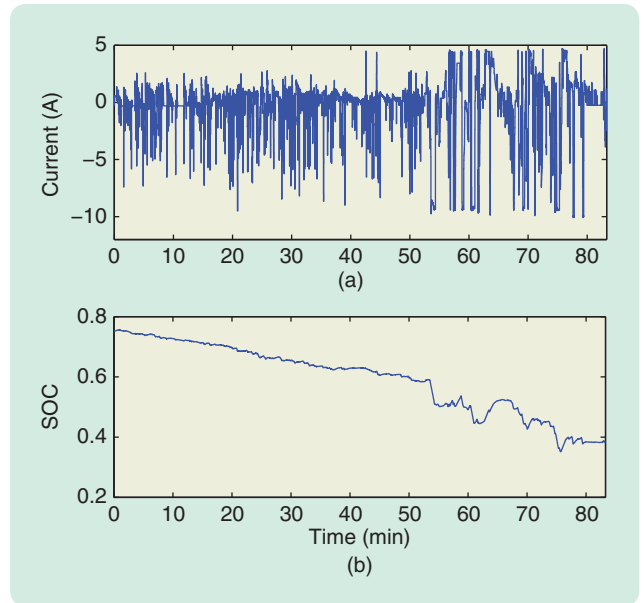


FIGURE 9 (a) Applied current and (b) time evolution of the bulk state of charge (SOC) of the 18650 cell. The current applied to the 18650 cell, as calculated from a measured power profile of a hybrid electric vehicle driving aggressively in the city and on a German highway, is depicted in (a). As shown in (a), the applied current is as high as 10 A in discharge and more than 4 A in charge. The 18650 cell has a nominal capacity of around 1.5 A-h. In (b), we present the corresponding bulk SOC swing (from a maximum of 0.76 to a minimum of 0.35) for the applied current, where the initial bulk SOC is normalized to be one at the rest voltage 4.2 V and zero at the rest voltage 2.8 V.

The design of a sophisticated BMS is necessary to ensure longevity and performance since battery behavior can change with time.

with a longer duration. This behavior is expected since the SPM does not model spatial variation of the states in the cell, including the variation of the electrolyte concentration. These spatial variations become more prominent in the cell for either large currents or for long-duration pulses.

Depending on accuracy requirements, these experimental results suggest that SPM might not be valid for the operating region encountered for EV applications. We next simulate the SPM for several rates of constant discharge currents to investigate its limitations as an approximation to the electrochemical model. A related comparison presented in [20] is based on only output voltage error for a high-power application cell, and error in states such as solid-phase concentration are not studied.

We next consider two sets of cells that include a high-power configuration with applications in HEVs, as well as a high-energy cell with applications in EVs and PHEVs. We compare output voltages computed from the two models, and also compare surface concentrations c_{ss} in the solid electrode. The comparison of surface concentration c_{ss} can then be used as an indicator of when the approximate model starts to fail.

High-Power Cell

We consider a high-power cell configuration with thin electrodes and separator. The nominal capacity of the cell is 1.5 A-h, and constant currents at C/5, 1 C, 5 C, and 10 C are applied (see “C Rate of a Current” for more details). The

corresponding voltages for the full electrochemical model and the SPM are shown in Figure 11, where the discharge curves are almost indistinguishable until 1 C. A similar result is reported in [20].

As shown in Figure 12, until 1 C the surface concentrations in the negative electrode are uniform, that is, $c_{ss}(x=0^-) \approx c_{ss}(x) \approx c_{ss}(x=L^-)$, with some transient deviations at mid-capacity discharge points. The surface concentration in SPM is the average surface concentration in the electrode. Since each electrode has only one node, the respective quantities at these nodes represent the average over the electrodes. At 5 C and 10 C, the uniformity in the concentration is lost, and the SPM is no longer valid. This failure of the approximation is noted in the corresponding rate plots in Figure 11. The difference between the surface concentrations at the two ends of the electrode ($x=0^-$ and $x=L^-$), in addition to being a function of the current density, is related to the slope of the OCP.

Finally, for a typical high-power application such as HEV or a power tool, the currents can be as high as 50 C for short durations. Thus, in these situations, a better approximation than SPM might be required.

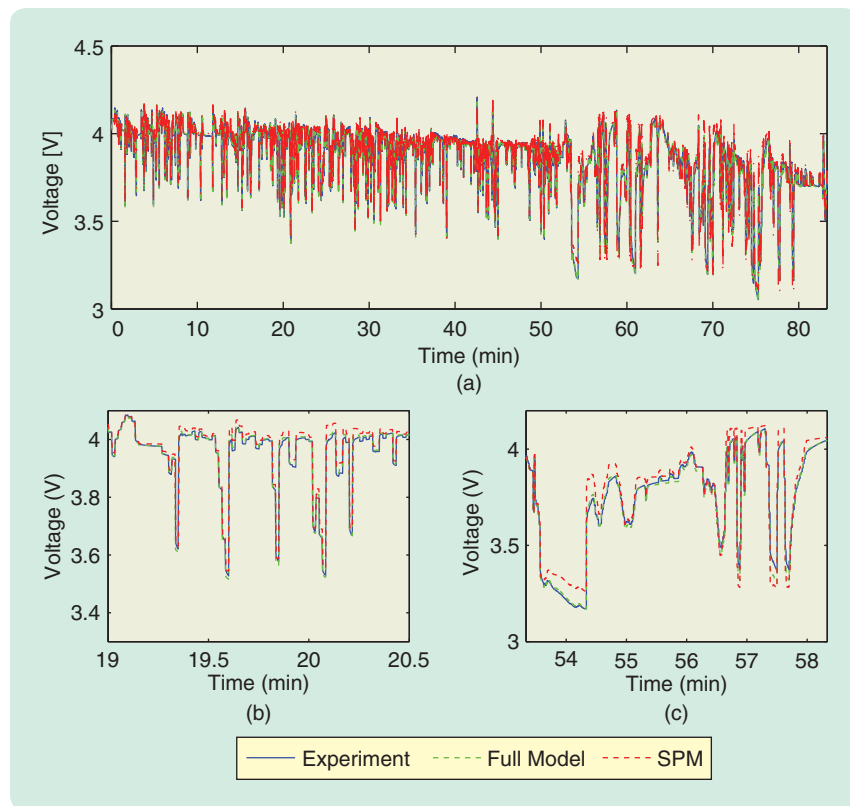


FIGURE 10 Comparison of the experimentally observed voltage response of a commercial 18650 cell with the full model and the single particle model (SPM). The full model matches the voltage response with a mean error of 13 mV. Compared to the full model, the SPM has a mean error of 28 mV, which is more than twice that of the full model. As shown in (a), (b), and (c), the errors in the SPM increase in magnitude for either large values of applied current, or during relaxation after applying a current pulse with a longer duration. These results suggest that the SPM is not able to model spatial variation of the states in the cell including those of electrolyte concentration. These spatial variations in the electrode become more prominent for either large currents or long-duration pulses.

High-Energy Cell

Similar to the high-power configuration case, we now compare the SPM with the full model for a high-energy cell configuration. Compared to the high-power cell, the electrodes of the high-energy cell are almost three times as thick, resulting in a cell with a nominal capacity of 3.5 A-h.

Similar to figures 11 and 12, the corresponding plots for the high-energy cell are given in figures 13 and 14, respectively. The applied currents are $C/25$, $C/2$, $1 C$, and $2 C$. The C rates of the applied currents for the high-energy cell are chosen lower compared to high-power cells. This choice of currents follows from the fact that, for high-energy applications such as in EVs, the C rates of the operating currents are usually lower compared to the high-power cell applications. Also, the cell capacity is larger, further reducing C rates of the current. However, transient currents may be expected to be as high as 4–5 C .

The plots for the high-energy cell in figures 13 and 14 show behavior similar to the high-power cell, except that the SPM model fails at currents above $C/2$. In fact, even at $C/2$, the variance in the surface concentrations shown in Figure 14 is large, suggesting that the SPM has significant errors in its prediction of cell states.

CURRENT STATUS AND FUTURE CHALLENGES FOR ADVANCED BMS

The design of a BMS for a Li-ion battery pack must address the complexity of the model of a Li-ion cell as well as the requirements for estimating states and parameters. A key feature of an advanced BMS is that it uses a physics-based electrochemical model instead of an equivalent circuit model. In contrast to equivalent circuit models (see “Equivalent Circuit Models in BMS”), alternative models are considered in [22], [27]–[29], [31], and [32], including electrochemical models. These models can

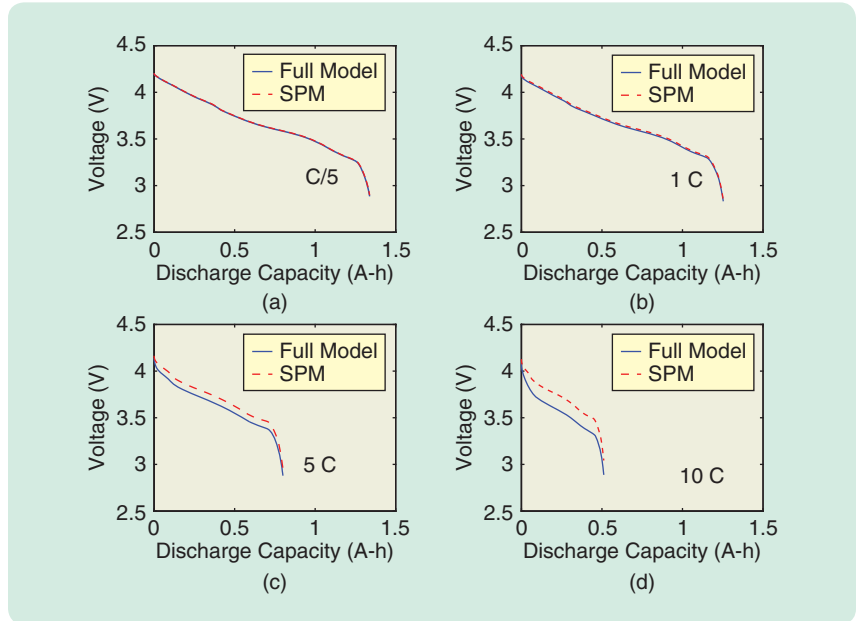


FIGURE 11 Comparison of the full model and the single particle model (SPM) for a high-power cell configuration. As shown in (a) and (b), the SPM performs acceptably until 1 C , after which the deviation between the full model and the SPM increases drastically. This deviation is expected since the SPM is based on the assumption that currents are small, and the electrolyte conductivity is large enough to avoid buildup of concentration gradients. Note that the SPM fails for higher currents in (c) and (d) since the concentration profiles in the electrode are no longer uniform, and hence the approximation of using a single particle is no longer valid.

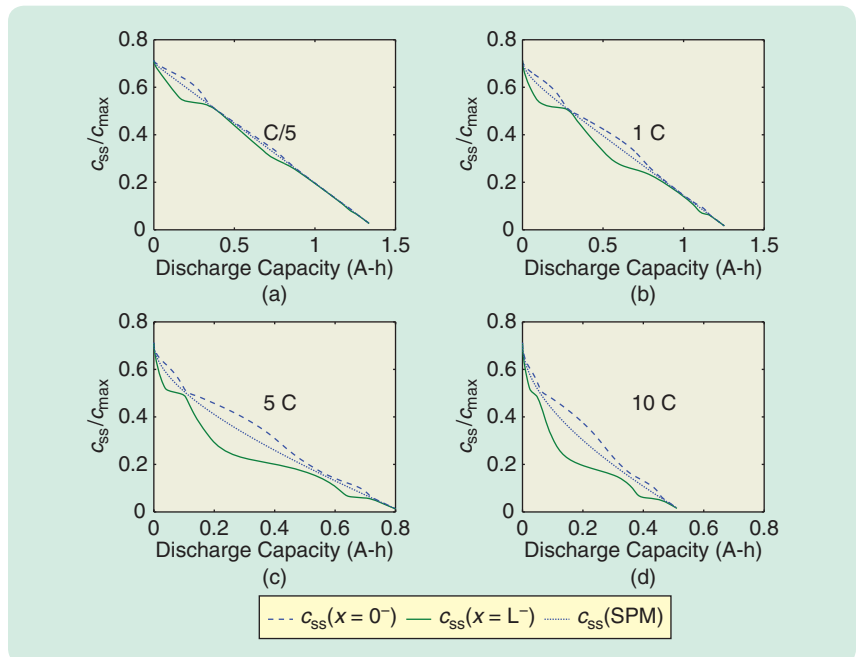


FIGURE 12 Surface concentrations computed from the electrochemical model and from the single particle model (SPM) for a high-power cell. As shown in (a) and (b), until 1 C current, the surface concentrations are uniform, that is, $c_{ss}(x=0^-) \approx c_{ss}(x=L^-)$, and the concentration computed from the SPM represents the mean of the value. However, for higher rates the uniformity breaks down, and the SPM is no longer a useful approximation, since the average concentration from the SPM does not capture the variation in kinetics in the electrode. As seen in (c) and (d), this breakdown of the approximation appears in the form of a large deviation in surface concentration over the electrode. Therefore, the SPM fails to predict the correct voltage for the rates 5 C and 10 C as shown in Figure 11.

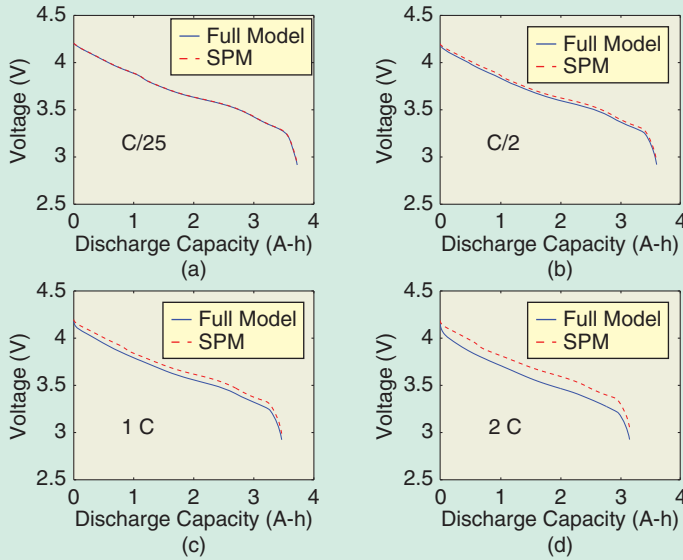


FIGURE 13 Comparison of the electrochemical model and the single particle model (SPM) for a high-energy cell. As seen in (a) and (b), the SPM is a useful approximation until $C/2$, above which the deviation between the electrochemical model and the SPM increases drastically. The failure observed in (c) and (d), at low C rates compared to high-power cells, is due to thicker electrodes in the high-energy cells yielding less nonuniform concentration profiles in the electrodes.

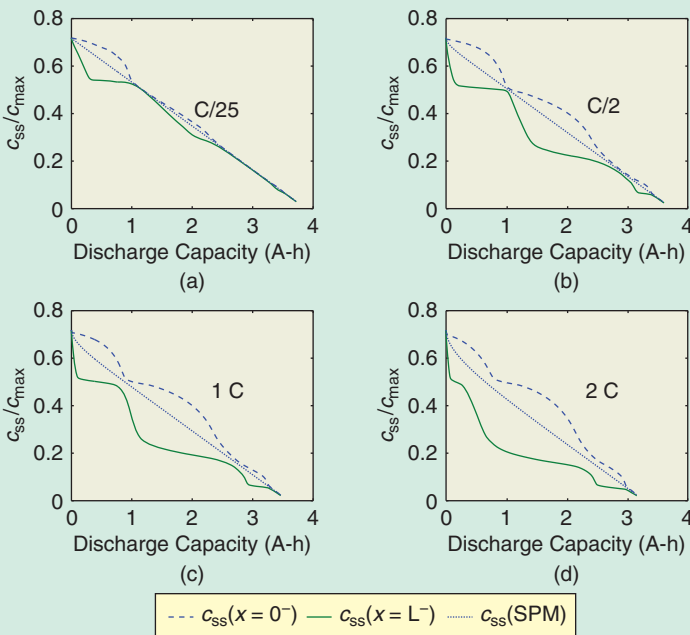


FIGURE 14 Surface concentrations computed from the electrochemical model and from the single particle model (SPM) for a high-energy cell. As shown in (a) and (b), the surface concentrations of the electrochemical model start to become nonuniform at $C/2$, and the concentration computed from the SPM represents the mean of the value. However, the large deviations between $c_{ss}(x=0^-)$ and $c_{ss}(x=L^-)$ suggest that the state information predicted by the SPM might be incorrect. As shown in (c) and (d), at higher rates (1 C and 2 C), the deviation in concentration compared to the mean concentration is large. Thus, the SPM fails to predict the correct voltage as shown in Figure 13.

be an empirical model with some electrochemical modeling information [31], [32], Laplace transform of the linearized electrochemical model [22], the single particle model [27], or an approximation based on either a modal deconstruction or model reformulation technique [28], [29].

Empirical models that include hysteresis are developed in [31] and [32]. As pointed out in [27], although empirical models can be used [31], [32], they suffer from the same limitation as equivalent circuits in that physical significance of the parameters is lost. Hence, physical insight into the battery is lost. In [22], Laplace transform methods in conjunction with linearization of Butler-Volmer kinetics (17) about a fixed SOC are used to identify approximate linear models. As expected, this model is less accurate over a large range of operation than the electrochemical model since it linearizes the Butler-Volmer kinetics and the OCP function. In [22], this problem is tackled by identifying the linear models at different operating points. While this nonlinear modification improves the performance of the model, it is subjected to the same limitations as those observed for equivalent circuit models, in that the physical significance of parameters is lost. In [27], a Kalman filter is designed for an approximate model based on SPM. This model is based on solving the PDE in the r -spatial domain given by (10) using an approximate polynomial expansion [33]. This approximation yields a further simplification of the SPM. As shown above, the SPM model itself is valid up to only 1 C current for high-power cells. Even for lower C rates, especially in high energy cells, this estimation approach might fail since, as shown in Figure 13, the SPM is no longer a useful approximation of the electrochemical model. POD or model reformulation methods are used in [28] and [29] to obtain cell models. However, compared to the SPM, models obtained by these methods are described by a

Equivalent Circuit Models in BMS

In [3], [6], and [8]–[11], an equivalent circuit model is used for the design of the BMS. This choice is primarily due to the early prevalence of BMS for portable electronics, where the approximation of the battery model with an equivalent circuit model is adequate. This modeling approach is then extended to Li-ion batteries for automotive or similar energy storage applications. Unfortunately, direct transplantation of the equivalent circuit-based BMS from portable electronics to the automotive application area can expose it to two serious pitfalls. First, the theoretical basis for equivalent circuit models is based on the response of the battery to a low-amplitude ac signal. Thus, equivalent circuit models have limited usefulness for automotive applications, where higher accuracy is required compared to portable electronic applications, especially during operations involving both *microcycling* and *deep cycling*. The operational regime of a battery involving high

current charge/discharge pulses with small change in SOC is called *microcycling*, whereas *deep cycling* corresponds to an operational regime involving low current pulses with large SOC changes.

As in linearization techniques, the equivalent circuit model can be extended by letting the circuit parameters depend on SOC [8]–[11] and temperature, or even the applied current. However, this approach yields the second pitfall, wherein a large number of parameters is needed to fit the equivalent circuit model. Thus, the complex electrochemical model of a battery is replaced by a complicated equivalent circuit model due to the variation of parameters that need fitting as functions of current, temperature, and SOC. Furthermore, since these parameters turn into mere *fitting* parameters for the model, the physical intuition behind the meaning of these parameters in an equivalent circuit model is lost.

large set of differential algebraic equations that need to be solved in real time for the BMS and require high-fidelity numerical solutions to capture the dynamics of the battery as it ages.

Independent of the scope of the work, [22], [27]–[29], [31], and [32] suggest using approximations of electrochemical models, or alternative physics-based models, to improve the accuracy of estimation algorithms for the BMS. As shown in the section “Framework for the Li-Ion Battery Model,” the Li-ion battery model consists of the diffusion equations (4) and (10) with flux j_n as the source and boundary condition, respectively. Thus, estimation or control techniques developed for parabolic PDEs [34] can potentially address these problems for the Li-ion battery. However, the coupling between the two PDEs through j_n inhibits the straightforward implementation of techniques studied in [34].

With this picture in mind, we mention future work that needs to be addressed for the design of improved and sophisticated BMS. Referring to the section “Control and Estimation Challenges for Li-Ion Batteries,” the future challenges are characterization of an approximation, that is, reduction of the full electrochemical model given by PDEs (4) and (10), and the algebraic equations (31) and (35), such that the model is simple enough to be analytically tractable and, yet, is as accurate as the electrochemical model. Retaining the physical significance of the parameters is critically essential since it helps in characterizing aging phenomena in batteries. Since the electrochemical model has physical parameters that are difficult and time consuming to identify, a quick offline estimation strategy to identify these parameters for new cell chemistries is required. Next, the design of simple algorithms for observing states of this model is an open problem, especially when applied to a battery pack

and not just one cell. Finally, real-time estimation of all parameters of the model and online identification of the state of health of the pack by tracking relevant physical parameters is an open problem.

AUTHOR INFORMATION

Nalin A. Chaturvedi (nalin.chaturvedi@us.bosch.com) received the B.Tech. and M.Tech. degrees in aerospace engineering from the Indian Institute of Technology, Bombay, in 2003, where he received the Institute Silver Medal. He received the M.S. degree in mathematics and the Ph.D. degree in aerospace engineering from the University of Michigan, Ann Arbor, in 2007. He was awarded the Ivor K. McIvor Award in recognition of research in applied mechanics. He is currently with the Research and Technology Center of the Robert Bosch LLC, Palo Alto, California. He is a member of the Energy Systems (ES) subcommittee within the mechatronics technical committee of the ASME Dynamic Systems and Controls Division. He is a visiting scientist at The University of California, San Diego. His current interests include model-based control for complex physical systems involving thermal-chemical-fluid interactions, nonlinear dynamical systems, state estimation, and adaptive control with applications to systems governed by PDEs. He can be contacted at Robert Bosch LLC, Research and Technology Center, 4009 Miranda Avenue, Palo Alto, California 94089, USA.

Reinhardt Klein received the Dipl.-Ing. degree in cybernetics engineering from the University of Stuttgart, Germany, in 2009. He is currently pursuing the Ph.D. degree at the Otto von Guericke University, Magdeburg. His interests include state estimation and adaptive control for systems governed by nonlinear DAEs and PDEs.

Jake Christensen received the B.S. in chemical engineering from the California Institute of Technology in 1998. He received the Ph.D. in chemical engineering from the University of California, Berkeley, in 2005. He is currently with the Research and Technology Center of the Robert Bosch LLC, Palo Alto, California. His interests include modeling and optimization of Li-ion battery systems.

Jasim Ahmed received the Ph.D. with a focus on spacecraft control from the University of Michigan, Ann Arbor, in 2000. He is currently with the Research and Technology Center of the Robert Bosch LLC, Palo Alto, California. His interests include the development of model-based control for complex physical systems involving thermal-chemical-fluid interactions.

Aleksandar Kojic received the B.Sc. from the Mechanical Engineering Department of the University of Kragujevac, Serbia, and the M.S.M.E. and Ph.D. from the Mechanical Engineering Department at the Massachusetts Institute of Technology, Cambridge, in 1995, 1998, and 2001, respectively. He is currently with the Research and Technology Center of Robert Bosch LLC, Palo Alto, California. His research interests are in the area of energy storage and conversion systems.

REFERENCES

- [1] J.-M. Tarascon and M. Armand, "Issues and challenges facing rechargeable lithium batteries," *Nature*, vol. 414, pp. 359–367, 2001.
- [2] M. Armand and J.-M. Tarascon, "Building better batteries," *Nature*, vol. 451, pp. 652–657, 2008.
- [3] T. Stuart, F. Fang, X. Wang, C. Ashtiani, and A. Pesaran, "A modular battery management system for HEVs," in *Proc. SAE Future Car Congr.*, 2002, 2002-01-1918.
- [4] D. Abraham, J. Liu, C. Chen, Y. Hyung, M. Stoll, N. Elsen, S. MacLaren, R. Twisten, R. Haasch, E. Sammann, I. Petrov, K. Amine, and G. Henriksen, "Diagnosis of power fade mechanisms in high-power lithium-ion cells," *J. Power Sources*, vol. 119–121, pp. 511–516, 2003.
- [5] I. Bloom, B. Potter, C. Johnson, K. Gering, and J. Christophersen, "Effect of cathode composition on impedance rise in high-power lithium-ion cells: Long-term aging results," *J. Power Sources*, vol. 155, pp. 415–419, 2006.
- [6] Y.-S. Lee and M.-W. Cheng, "Intelligent control battery equalization for series connected lithium-ion battery strings," *IEEE Trans. Ind. Electron.*, vol. 52, no. 5, pp. 1297–1307, 2005.
- [7] D. H. Doughty and C. C. Crafts. (2006). *FreedomCAR Electrical Energy Storage System Abuse Test Manual for Electric and Hybrid Electric Vehicle Applications*. Sandia National Laboratories, Albuquerque, NM [Online]. Available: http://www.prod.sandia.gov/cgi-bin/techlib/access-control.pl/2005/05312_3.pdf
- [8] M. W. Verbrugge and R. S. Conell, "Electrochemical and thermal characterization of battery modules commensurate with electric vehicle integration," *J. Electrochem. Soc.*, vol. 149, no. 1, pp. A45–A53, 2002.
- [9] B. Schweighofer, K. M. Raab, and G. Brasseur, "Modeling of high power automotive batteries by the use of an automated test system," *IEEE Trans. Instrum. Meas.*, vol. 52, no. 4, pp. 1087–1091, 2003.
- [10] M. Chen and G. A. Rincón-Mora, "Accurate electrical battery model capable of predicting runtime and I-V performance," *IEEE Trans. Energy Conversion*, vol. 21, no. 2, pp. 504–511, 2006.
- [11] M. W. Verbrugge and R. S. Conell, "Electrochemical characterization of high-power lithium ion batteries using triangular voltage and current excitation sources," *J. Power Sources*, vol. 174, no. 1, pp. 2–8, 2007.
- [12] J. Newman and W. Tiedemann, "Porous-electrode theory with battery applications," *AICHE J.*, vol. 21, no. 1, pp. 25–41, 1975.
- [13] M. Doyle, T. F. Fuller, and J. Newman, "Modeling of galvanostatic charge and discharge of the lithium/polymer/insertion cell," *J. Electrochem. Soc.*, vol. 140, no. 6, pp. 1526–1533, 1993.
- [14] T. F. Fuller, M. Doyle, and J. Newman, "Simulation and optimization of the dual lithium ion insertion cell," *J. Electrochem. Soc.*, vol. 141, pp. 1–10, 1994.
- [15] K. Thomas, J. Newman, and R. Darling, *Advances in Lithium-Ion Batteries: Mathematical Modeling of Lithium Batteries*. New York: Springer-Verlag, 2002.
- [16] J. Newman and K. E. Thomas-Aleya, *Electrochemical Systems*. Hoboken, NJ: Wiley, 2004.
- [17] I. J. Ong and J. Newman, "Double-layer capacitance in a dual lithium ion insertion cell," *J. Electrochem. Soc.*, vol. 146, no. 12, pp. 4360–4365, 1999.
- [18] A. J. Bard and L. R. Faulkner, *Electrochemical Methods: Fundamentals and Applications*. New York: Wiley, 2001.
- [19] G. Ning and B. N. Popov, "Cycle life modeling of lithium-ion batteries," *J. Electrochem. Soc.*, vol. 151, no. 10, pp. A1584–A1591, 2004.
- [20] S. Santhanagopalan, Q. Guo, P. Ramadass, and R. E. White, "Review of models for predicting the cycling performance of lithium ion batteries," *J. Power Sources*, vol. 156, no. 2, pp. 620–628, 2006.
- [21] K. Smith and C.-Y. Wang, "Power and thermal characterization of a lithium-ion battery pack for hybrid electric vehicles," *J. Power Sources*, vol. 160, no. 1, pp. 662–673, 2006.
- [22] K. Smith, C. Rahn, and C.-Y. Wang, "Control oriented 1D electrochemical model of lithium ion battery," *Energy Convers. Manage.*, vol. 48, no. 9, pp. 2565–2578, 2007.
- [23] A. Pesaran, T. Markel, H. Tataria, and D. Howell. (2007). Battery requirements for plug-in hybrid electric vehicles—Analysis and rationale. *Proc. 23rd Int. Electric Vehicle Symp. (EVS-23)* [Online]. Available: <http://www.nrel.gov/vehiclesandfuels/energystorage/pdfs/42240.pdf>
- [24] P. Arora, M. Doyle, and R. E. White, "Mathematical modeling of the lithium deposition overcharge reaction in lithium-ion batteries using carbon-based negative electrodes," *J. Electrochem. Soc.*, vol. 146, no. 10, pp. 3543–3553, 1999.
- [25] J. Christensen and J. Newman, "Cyclable lithium and capacity loss in Li-ion cells," *J. Electrochem. Soc.*, vol. 152, no. 4, pp. A818–A829, 2005.
- [26] L. C. Evans, *Partial Differential Equations* (Graduate Studies in Mathematics). Providence, RI: American Mathematical Society, 1998.
- [27] S. Santhanagopalan and R. E. White, "Online estimation of the state of charge of a lithium ion cell," *J. Power Sources*, vol. 161, no. 2, pp. 1346–1355, 2006.
- [28] L. Cai and R. White, "Reduction of model order based on proper orthogonal decomposition for lithium-ion battery simulations," *J. Electrochem. Soc.*, vol. 156, no. 3, pp. A154–A161, 2009.
- [29] V. Subramanian, V. Boovaragavan, V. Ramadesigan, and M. Arabandi, "Mathematical model reformulation for lithium-ion battery simulations: Galvanostatic boundary conditions," *J. Electrochem. Soc.*, vol. 156, no. 4, pp. A260–A271, 2009.
- [30] C. Motloch, J. Christophersen, J. Belt, R. Wright, G. Hunt, R. Sutula, T. Duong, T. Tartamella, H. Haskins, and T. Miller, "PNGV battery testing procedures and analytical methodologies for HEVs," in *Proc. SAE Future Car Congr.*, 2002, 2002-01-1950.
- [31] G. L. Plett, "Extended Kalman filtering for battery management systems of LiPB-based HEV battery packs: Part 2. Modeling and identification," *J. Power Sources*, vol. 134, no. 2, pp. 262–276, 2004.
- [32] G. L. Plett, "Extended Kalman filtering for battery management systems of LiPB-based HEV battery packs: Part 3. State and parameter estimation," *J. Power Sources*, vol. 134, no. 2, pp. 277–292, 2004.
- [33] V. R. Subramanian, V. D. Diwakar, and D. Tapriyal, "Efficient macro-micro scale coupled modeling of batteries," *J. Electrochem. Soc.*, vol. 152, no. 10, pp. A2002–A2008, 2005.
- [34] M. Krstic and A. Smyshlyayev, *Boundary Control of PDEs: A Course on Backstepping Designs*. Philadelphia, PA: SIAM, 2008.

